Journal of Cleaner Production 434 (2024) 139794

Contents lists available at ScienceDirect

Journal of Cleaner Production

journal homepage: www.elsevier.com/locate/jclepro

Enhancing the resilience of zero-carbon energy communities: Leveraging network reconfiguration and effective load carrying capability quantification

Abdollah Younesi [a], Zongjie Wang [a,*], Pierluigi Siano [b,c]

[a] Department of Electrical and Computer Engineering, Eversource Energy Center, University of Connecticut Connecticut, USA
[b] Department of Management & Innovation Systems, University of Salerno, Italy
[c] National University of Science and Technology POLITEHNICA Bucharest, Romania

ARTICLE INFO

Handling Editor: Jin-Kuk Kim

Keywords:
Energy communities
Grid resilience
Effective load carrying capability
Extreme events
Mesh-view mapping
Network reconfiguration

ABSTRACT

The integration of distributed energy resources (DERs) into contemporary energy communities (ECs) has revolutionized power systems, fostering sustainable and clean energy infrastructures. This paper focuses on the effective load-carrying capability (ELCC) to enhance grid resilience in the presence of DERs. We introduce an innovative network topology-based optimization framework that seamlessly integrates economic and resilience metrics within ECs while reducing carbon emissions. The Pareto front of non-dominated solutions for the proposed three-objective optimization problems is extracted, providing a comprehensive visualization of the trade-off between economic, resilience, and emission objectives, enabling informed decision-making. Analytical results, validated on the IEEE 33-bus test system, demonstrate the effectiveness of DER-based ELCC quantification in managing load supply during emergencies. Case studies show how the synergy between economic and resilience-based metrics significantly enhances grid resilience. The proposed framework has diverse applications, including enhancing grid adaptability to climate change, promoting sustainable energy integration, optimizing demand response strategies, and supporting the transition to a decarbonized energy community. This work addresses the challenges and opportunities in the evolving energy landscape, emphasizing the importance of our approach in achieving a cleaner and more resilient energy future.

1. Introduction

The evolution of the power system increased sustainability, reliability, and resilience is driven by the development of contemporary ECs with higher levels of clean and renewable DERs. Planning urban areas for positive energy transformation, focusing on decarbonization and renewable energy deployment, requires a long-term perspective, active engagement of various societal elements, and an inclusive approach to prevent inequality while promoting the development of positive energy communities (Lazaroiu and Putrus, 2023). In fact, ECs enable both DERs and customers to actively participate in energy management, leading to social, environmental, and economic benefits while fostering innovative management strategies within the power system (Nagpal et al., 2022). Besides providing innovative energy management solutions to distribution system operators (DSOs), ECs also hold significant potential for enhancing power system capabilities in addressing high-impact low-probability (HILP) events (Younesi et al., 2022a). In other words, by appropriately allocating DERs close to load centers, the dependency on power transfer through power lines (which are the most vulnerable components facing HILP events) is reduced, ultimately improving grid resilience (Younesi et al., 2020).

Over time, the HILP events have increased in frequency due to climate change. Although addressing environmental factors in long-term planning can help reduce the occurrence of HILP events, it remains crucial for power systems to be adequately prepared in the short term (Younesi et al., 2023). This preparation involves hardware upgrades and operational planning strategies to effectively manage such events. As a result, numerous advancements have been made to assess and enhance grid resilience against HILP events, emphasizing the importance of both short-term and long-term planning in the face of a changing climate (Mahzarnia et al., 2020; Younesi et al., 2022a; Wang et al., 2015).

In practice, dividing the distribution system into multiple local ECs offers significant potential to satisfy both DSO and end-user customers in the short term from both economic and resilience perspectives. As such, this transition is of paramount importance and cannot be overlooked, necessitating the thorough assessment and enhancement of resilience within these ECs. In addition, the aggregation and optimal dispatch of DERs play a critical role in ECs, contributing to enhanced resilience while optimizing operational costs. A hierarchical control

* Corresponding author.
E-mail address: zongjie.wang@uconn.edu (Z. Wang).

https://doi.org/10.1016/j.jclepro.2023.139794
Received 9 October 2023; Received in revised form 2 November 2023; Accepted 15 November 2023
Available online 25 November 2023

Nomenclature

Acronyms

$H\&N$	*Here-and-now*
$W\&S$	*Wait-and-see*
CE	*Carbon emission*
DA	*Day-ahead*
DER	*Distributed energy resource*
DG	*Distributed generation*
DSO	*Distribution system operator*
EC	*Energy community*
ELCC	*Effective load-carrying capability*
ESS	*Energy storage system*
EV	*Electric vehicle*
EVP	*Electric vehicle parking*
FI	*Fragility index*
HILP	*High-impact low-probability*
LEI	*Lost energy index*
LOLE	*Loss of load expectation*
LOLP	*Loss of load probability*
MISO	*Midcontinent independent system operator*
REI	*Restoration efficiency index*
RT	*Real-time*
SOC	*State-of-charge*
TSERS	*Two-stage economic-resilience scheduling*
VDI	*Voltage deviation index*

Indices & Symbols

ω	*Index of scenario*
n, r	*Index of bus*
$\boldsymbol{X}_{\mathrm{H\&N}}$	*H&N vector of the decision variables*
$\boldsymbol{x}_{\mathrm{W\&S}}$	*W&S vector of the decision variables*
i	*Index of breakpoints in piecewise linear approximation*
t	*Index of hours*

Parameters

κ_n	*Auxiliary parameter*
λ^{DG}	*Start-up cost of DG*
λ^{G}_{nt}	*DG operational cost*
λ^{L}_{nt}	*H&N customers-side energy price*
$\lambda^{R,dep}_{nt}$	*Price of deploying demand-side reserve*
λ^{sh}_{nt}	*Load shedding cost*
$\lambda^{u(d)}_{nt}$	*The price of up (down) reserves*
ν_{ω}	*Probability of scenario*
$\rho^{b(s)}$	*H&N Energy price for the buyer (seller)*
$\rho^{w\&s,b+(-)}_{t\omega}$	*w&S correction of the price for buyers*
$\rho^{w\&s,E}_{t\omega}$	*Price of energy storage device power*
$\rho^{w\&s,G}_{t\omega}$	*Price of DG spinning reserve*
$\rho^{w\&s,s+(-)}_{t\omega}$	*w&S correction of the price for sellers*
$\rho^{w\&s,W}_{t\omega}$	*Price of buying wind energy*
$a(b)$	*H&N (W&S) Status of EVP*
$G(B)$	*The admittance real (imaginary) parts*
N_{Γ}	*Number of Scenarios*
N_{bus}	*Total system buses*
$PC(t)$	*Energy community performance curve*
PC_p	*Pre-event performance curve*
PC_{pr}	*Post-restoration performance curve*
Q^{C}_{n}	*Compensator capacity*
t_{es}	*Event start time*
t_{ire}	*Infrastructure restoration end time*
t_{rs}	*Restoration start time*
z	*Islanding mode indicator of MG*
$Z^{P(Q)}, I^{P(Q)}, P^{P(Q)}$	*The coefficients of the ZIP model of the load*
CI^{up}_{t}	*The H$N generated carbon at the upstream network for importing each kWh*
$h^{1(2)}$	*Piecewise linear approximation coefficients*
M_1, M_2	*Positive large number*
N_t	*Scheduling time horizon (Hours)*
$P_{e,\omega}$	Probability of occurring event e in scenario ω
PC_{pe}	*Post-event performance curve*
t_d	*Degradation start time*
t_{ed}	*Event end time*
t_{irs}	*Infrastructure restoration start time*
t_{re}	*Restoration end time*
V^{*}_{n}	*The scheduled voltage of bus n*

Variables

$\Delta p^{b+(-)}_{t\omega}$	*w&S correction of the power of buyers*
$\Delta p^{s+(-)}_{t\omega}$	*w&S correction of the power of sellers*
γ^{c}	*Compensator step*
$\psi^{stg(EV)}$	*H&N state of energy storage (electric vehicle) systems*
θ_n	*Voltage angle*
c^{s}_{ntw}	*DG starting cost*
$CE^{H\&N,up}_{t}$	*Total H&N generated carbon emission related to the upstream network*
CI^{G}_{nt}	*The H$N generated carbon for injecting each kWh from DGs*
$fl^{P(Q)}$	*Active (Reactive) power flow*
$P^{b(s)}$	*H&N scheduled power for buyer (seller)*
$p^{B,E}_{nt\omega}$	*w&S power of energy storage devices*
$p^{B,G}_{nt\omega}$	*w&S purchased DG spinning reserve*
$p^{B,W}_{nt\omega}$	*w&S power of wind energy*
$p^{G}_{nt\omega}$	*w&S power of DG*
$p^{Shed}_{nt\omega}$, $q^{Shed}_{nt\omega}$	*Active and reactive load curtailments*
$p^{sh}_{nt\omega}$	*w&S shedding load*
$P^{E+(-)}_{nt}$	*H&N charge(discharge) power of energy storage system*
$P^{EV+(-)}_{nt}$	*H&N charge(discharge) power of electric vehicle*
P^{G}_{nt}	*H&N power of DG*
P^{L}_{nt}	*H&N active load*
P^{L}_{nt}	*H&N load power*
P^{W}_{nt}	*H&N wind power*

strategy was proposed in Utkarsh et al. (2021), wherein the flexibility and dispatch of DERs were optimized using convex optimization models. Social welfare, defined as end-user satisfaction with grid service, can be achieved as an optimization goal for DSO planning, ensuring that the needs of all stakeholders are met. In Putratama et al. (2022) the authors developed a three-level method that integrated day-ahead, real-time, and half-hourly basis horizons. The primary goal of this study was to reduce operational costs for households by implementing local ECs. From both economic and resilience perspectives, energy storage

$P_t^{H\&N,b(s)}$	*H&N purchased (sold) power from (to) the main grid*
$P_t^{H\&N}$	*H&N power exchange with main grid*
$r_{ntω}^{LU(D)}$	*w&S deployed demand-side reserve*
$R_{nt}^{u(d)}$	*Up (down) reserves*
$SOC^{E(EV)}$	*H&N state of the charge of energy storage (electric vehicle) systems*
V_n	*Voltage magnitude*
$\xi, x, y, \gtrless$	*Binary variables*
C	*The operational cost*
$C^{\mathrm{H\&N}}$	*H&N operational cost*
$c^{\mathrm{W\&S}}$	*W&S operational cost*
c_t^d	Cost of buying energy from DERs and demand side reserves
c_t^u	Cost of power exchange with the upstream network
$CE_t^{H\&N,G}$	*Total H&N generated carbon emission related to the DGs*
f_1	*The economic objective function*

systems offer significant benefits to the distribution system, encompassing all renewable/dispatchable DERs, prosumers, and consumers. In Vespermann et al. (2020), it was demonstrated that all market players benefit from storage devices, even without direct ownership. Moreover, the placement and sizing of DERs, along with network reconfiguration, were proposed in Rahiminejad et al. (2023) to enhance resilience against cyber-attacks.

Energy communities involve consumers with DERs. These communities experiment with new energy practices, such as local flexibility markets and cooperative microgrids, to achieve energy resilience. Tomin et al. (2022) presented a modeling framework using bilevel programming and reinforcement learning for optimizing community microgrid management, resulting in cost reduction and improved electricity supply quality for settlements and resilience. In addition to bolstering grid resilience through the inclusion of DERs and storage facilities, ECs also benefit from flexible loads. These loads enable DSOs to prioritize the continuous operation of critical loads during emergency events. A new bi-level method was proposed in Chamana et al. (2022) to manage controllable devices in a small microgrid, ensuring that loads were supplied in priority order. A post-disaster recovery method using portable energy resources, electric vehicles, and energy storage devices was later proposed in Papari et al. (2021), employing network reconfiguration to improve the microgrid community resilience. Inherent uncertainties of demand response for flexible loads and renewable resources in microgrid communities have raised concerns for planners regarding short-term and long-term resilience against disasters. To tackle this issue, Guo et al. (2019) proposed a short-term stochastic, resilience-oriented network reconfiguration method that took into account the impact of demand response, with disaster costs as the primary objective function. Furthermore, a long-term risk-based planning mechanism for active distribution systems was further developed to improve resilience in Poudyal et al. (2022). While grid resilience has been the focus of the aforementioned studies, the resilience metrics have not been directly incorporated into the objective functions of the optimization process. This omission has led to concerns that resilience-based optimal solutions may not be backed by a strong theoretical foundation. To address this, it is necessary to seamlessly integrate resilience metrics within the optimization process, thereby establishing a more robust approach to achieving optimal solutions that effectively improve grid resilience.

From the literature review above, it is evident that the effective load-carrying capability (ELCC) (Midcontinent-ISO, 2015), which quantifies the capacity contribution for generation outputs such as wind and solar, has not been explored in the context of ***resilience assessment*** for the distribution system. The ELCC of renewable sources refers to the measure of incremental load that they can consistently support over a prolonged period. This concept has been widely recognized and implemented by the Midcontinent Independent System Operator (MISO), which has employed the ELCC credit values of wind and solar in their resource adequacy process for numerous years (Heath and Figueroa-Acevedo, 2018). In fact, ECs with higher ELCC credit, particularly those with DER-based ELCC, possess greater capabilities in restoring critical loads following a disaster. The concept of defining the capacity of DGs to support additional demand without necessitating new units was first introduced as a sustainability factor in the power system in Dent et al. (2014). This attribute can be utilized in resilience enhancement programs for distribution systems, enabling a rapid restoration process after an incident. However, uncertainties arising from renewable energy sources introduce more significant challenges to the distribution system, complicating the process of calculating the corresponding ELCC values. To address this issue, an approximated dynamic programming method was proposed in Chen et al. (2014) for calculating the ELCC of renewable energy resources on an hourly basis. The significance of shifting to renewable energy sources due to the substantial role of fossil fuels in global greenhouse gas emissions is underlined in Osman et al. (2023). The paper discusses the impact of climate change on renewables, highlights the decreasing costs of solar and wind energy, and emphasizes the potential for renewable energy to decarbonize the electricity sector and mitigate climate change. To the best of the authors' knowledge, the creation of mathematical models that effectively integrate and quantify the ELCC within the resilience enhancement process remains an intricate and uncharted territory. This highlights the need for continued research and development in this area to devise innovative approaches that leverage the potential of ELCC, ultimately leading to a more resilient and robust power system in the face of uncertainties from renewable energy sources. In order to distinguish the novelties of the current paper from previous papers, the literature review is summarized in Table 1.

Drawing from the comprehensive literature review, it is evident that while the advantages of Energy Communities (ECs) and Effective Load-Carrying Capability (ELCC) credits for grid resilience are well-recognized, a distinct challenge persists. This challenge revolves around the development of robust mathematical formulations that seamlessly integrate DER-based ELCC credits into the framework for enhancing EC resilience. To bridge this crucial gap, this paper introduces a theoretical analysis of the incorporation of DER-based ELCC credits into EC resilience enhancement, employing post-event network reconfiguration strategies. To achieve this objective, a sophisticated two-stage algorithm is presented, effectively integrating economic, resilience, and carbon emission metrics within the integrated ECs. This approach ensures the optimality of the objective function while maintaining resilience under varying loading conditions. Moreover, we introduce an innovative mesh-view grid mapping structure, devised by the authors, to evaluate EC model behavior during extreme events, thereby assessing resilience comprehensively. In addition to these advancements, carbon emission-related constraints are integrated into the operational constraints of the system, promoting environmentally friendly practices. The paper culminates with a series of simulation case studies conducted on the IEEE 33-bus test system, which conclusively demonstrate the effectiveness and efficiency of the proposed framework. Notably, one of the primary contributions of this research lies in the extraction of the Pareto front of non-dominated solutions for the proposed three-objective optimization problem. This analytical process provides a holistic visualization of the trade-off between economic, resilience, and emission objectives, offering decision-makers the essential insights to make well-informed decisions tailored to their specific requirements and preferences. In summary, this paper addresses the critical gap in integrating DER-based ELCC credits into EC resilience enhancement, offering a refined mathematical framework and employing innovative

Table 1
Comparison between the present article and previous literature.

Ref. No.	Economic index	Resilience index	Emission index	Tri-objective	DER based ELCC	Reconfiguration	Uncertainties
Younesi et al. (2023)	Yes	Yes	Yes	No	No	No	Yes
Utkarsh et al. (2021)	Yes	Yes	No	No	No	No	No
Putratama et al. (2022)	Yes	No	No	No	No	No	Yes
Vespermann et al. (2020)	Yes	No	No	No	No	No	No
Rahiminejad et al. (2023)	Yes	Yes	No	No	No	Yes	No
Tomin et al. (2022)	Yes	No	Yes	No	No	No	Yes
Chamana et al. (2022)	No	Yes	No	No	No	No	Yes
Papari et al. (2021)	Yes	Yes	No	No	No	Yes	No
Guo et al. (2019)	Yes	Yes	No	No	No	No	Yes
Poudyal et al. (2022)	Yes	Yes	No	No	No	No	Yes
Younesi et al. (2022b)	Yes	Yes	No	No	No	No	Yes
Current paper	**Yes**	**Yes**	**Yes**	**Yes**	**Yes**	**Yes**	**Yes**

methodologies. The introduction of carbon emission constraints and the extraction of the Pareto front further enrich the paper's contributions. Specifically, the main contributions of this paper can be summarized as follows:

- Evaluate the impact of the DER-based ELCC credit on grid resilience under the implementation of the mesh-view grid mapping structure;
- Extracting the Pareto front of non-dominated solutions for providing a comprehensive visualization of the economic-resilience-emission trade-off for informed decision-making;
- Develop an innovative approach for improving the assessment of resilience in large-scale energy communities, taking into account network reconfiguration strategies following events;
- Incorporate carbon emission constraints into the stochastic scheduling framework that combines grid economics and resilience for a decarbonized energy community;
- Accounting for uncertainties in renewable generation, market prices, and event characteristics (including location, type, and severity level) to make the results more realistic.

The structure of this paper is organized as follows. In Section 2, a comprehensive and theoretical-based methodology is proposed, encompassing various components. Firstly, a generalized two-stage economic-resilience scheduling (TSERS) framework is introduced in Section 2.1. The ELCC quantification procedure is discussed in Section 2.2. Section 2.3 presents the integration of ELCC with the TSERS framework. Additionally, II-D delves into the event characteristics analysis using the innovative mesh-view grid mapping structure. Section 3 conducts the simulation case studies on the IEEE 33-bus test system. Section 4 concludes the paper by summarizing the findings and suggesting potential avenues for future work.

2. Methodology

In this section, a generalized economic-resilience-based two-objective two-stage stochastic scheduling formulation for ECs is first provided. The DER-based ELCC method is then defined, qualified, and integrated into the general TSERS framework.

2.1. Generalized two-stage economic-resilience scheduling (TSERS)

2.1.1. Economic objective function

The proposed generalized TSERS consists of two stages, which are referred to as either *here-and-now* (***H&N***) and *wait-and-see* (***W&S***) or *day-ahead* (***DA***) and *real-time* (***RT***). For consistency, the first stage is denoted as ***H&N***, and the second stage as ***W&S*** in this paper. Furthermore, uppercase and lowercase letters are utilized to represent variables in ***H&N*** and ***W&S***, respectively. Let $\boldsymbol{X}_{\mathrm{H\&N}}$ and $\boldsymbol{x}_{\mathrm{W\&S}}$ be the corresponding vectors of decision variables representing each stage. The cost under the economic objective function (i.e., f_1) associated with both *H&N* and *W&S* variables is presented as follows:

$$f_1 = \sum_{t=t_0}^{N_t} C_t\left(\boldsymbol{X}_{H\&N}, \boldsymbol{x}_{W\&S}\right) = \sum_{t=t_0}^{N_t} (C_t^{H\&N} + c_t^{W\&S}). \tag{1}$$

$C^{H\&N}$ is calculated hourly and encompasses the cost of exchange with the upstream network, the cost of demand-side reserves, and the income generated from selling energy to customers. The expression for $C^{H\&N}$ is given in (2) (Younesi et al., 2021b).

$$C_t^{H\&N} = \rho_t^b\ P_t^b - \rho_t^s\ P_t^s + \sum_{n=1}^{N_{bus}} (\lambda_{nt}^u\ R_{nt}^u + \lambda_{nt}^d\ R_{nt}^d - \lambda_{nt}^L\ P_{nt}^L). \tag{2}$$

Similarly, $c^{W\&S}$ is calculated hourly in each scenario using (3). It encompasses the cost of power exchange with the upstream network (c_u), the cost of purchasing energy from independent DERs, the operational cost of supplying energy from dependent DERs, and the costs associated with demand-side reserves (c_d) (Younesi et al., 2021b).

$$c_t^{W\&S} = c_t^u + c_t^d, \tag{3}$$

where the term c_t^u represents the cost of adjustments in the day-ahead scheduled import/export power based on the real-time market prices, and it is expressed by (4).

$$\begin{aligned} c_t^u = \sum_{\omega=1}^{N_\Gamma} \nu_\omega \Big[& (\rho_{t\omega}^{w\&s,b+}\ \Delta p_{t\omega}^{b+}) \\ & -(\rho_{t\omega}^{w\&s,b-}\ \Delta p_{t\omega}^{b-}) - (\rho_{t\omega}^{w\&s,s+}\ \Delta p_{t\omega}^{s+}) + (\rho_{t\omega}^{w\&s,s-}\ \Delta p_{t\omega}^{s-}) \Big]. \end{aligned} \tag{4}$$

c_t^d represents the cost of purchasing energy from DERs and demand-side reserves, as given by (5).

$$\begin{aligned} c_t^d = \sum_{\omega=1}^{N_\Gamma} \sum_{n=1}^{N_{bus}} \nu_\omega \Big[& (c_{ntw}^s + \lambda_{nt}^G\ p_{nt\omega}^G) + (\rho_{t\omega}^{w\&s,W}\ p_{nt\omega}^{B,W}) \\ & +(\rho_{t\omega}^{w\&s,G}\ p_{nt\omega}^{B,G} + \lambda_{t\omega}^{w\&s,RG}\ r_{nt\omega}^{B,G}) + (\rho_{t\omega}^{w\&s,E}\ p_{nt\omega}^{B,E}) \\ & +(\lambda_{nt}^{R,dep}\ (r_{nt\omega}^{LU} - r_{nt\omega}^{LD})) + (\lambda_{nt}^{sh}\ p_{nt\omega}^{sh}) \Big]. \end{aligned} \tag{5}$$

The decision variables are subject to a set of constraints, which are modeled as equality, inequality, and bound constraints. Some of these constraints are related to the *H&N* and *W&S* stages, while others connect the variables of both stages.

2.1.2. H&N constraints

The *H&N* constraints are represented in (6)–(27). The active power balance of the EC is given by (6), in which the $P_t^{H\&N}$ is determined based on the amount of energy purchased from and sold to the main grid, as specified in (7).

$$P_t^{H\&N} = \sum_{n=1}^{N_{bus}} \left[P_{nt}^G + P_{nt}^W - (P_{nt}^{EV+} - P_{nt}^{EV-}) - (P_{nt}^{E+} - P_{nt}^{E-}) + P_{nt}^L\right]. \tag{6}$$

$$P_t^{H\&N} = P_t^{H\&N,b} - P_t^{H\&N,s}. \tag{7}$$

The amount of power exchanged with the main grid (either purchased or sold) is subject to limitations based on emissions and power shortages on both sides (i.e. the main grid and the local EC). These limitations are incorporated into the formulation through (8) and (9).

$$0 \le P_t^{H\&N,b} \le \overline{P}_t^{H\&N,b} \xi_t^{H\&N}. \tag{8}$$

$$0 \le P_t^{H\&N,s} \le \overline{P}_t^{H\&N,s} (1 - \xi_t^{H\&N}). \tag{9}$$

The power of DGs, WTs, and loads, as well as the reserve amount of system power, are constrained by physical limitations and techno-economic characteristics, as demonstrated in (10)–(14).

$$\underline{P}_n^G x_{nt} \le P_{nt}^G \le \overline{P}_n^G x_{nt}. \tag{10}$$

$$\underline{P}_n^W \le P_{nt}^W \le \overline{P}_n^W. \tag{11}$$

$$\underline{P}_n^L \le P_{nt}^L \le \overline{P}_n^L. \tag{12}$$

$$0 \le R_{nt}^{LU} \le \overline{R}_{nt}^{LU}. \tag{13}$$

$$0 \le R_{nt}^{LD} \le \overline{R}_{nt}^{LD}. \tag{14}$$

The operation of the energy storage system in the EC is modeled through several equations, including the state-of-charge (SOC) at each time step, as expressed in (15), the initial SOC in (16), the maximum/minimum level of SOC in (17), and the amount of charge/discharge at each time step, as described in (18) and (19).

$$SOC_{nt}^E = SOC_{n(t-1)}^E + \frac{\eta_n^E}{\overline{E}_n^E} P_{n(t-1)}^{E+} - \frac{1}{\eta_n^E \overline{E}_n^E} P_{n(t-1)}^{E-}. \tag{15}$$

$$SOC_{n(T_0)}^E = SOC_n^0. \tag{16}$$

$$\underline{SOC}_n^E \le SOC_{nt}^E \le \overline{SOC}_n^E. \tag{17}$$

$$0 \le P_{nt}^{E+} \le \overline{P}_{nt}^{E+} \psi_{nt}^E. \tag{18}$$

$$0 \le P_{nt}^{E-} \le \eta_n^E \overline{P}_{nt}^{E-} (1 - \psi_{nt}^E). \tag{19}$$

Electric vehicles (EVs) can be modeled similar to energy storage systems (ESSs). However, there are some minor differences in the behavior of charge/discharge of their batteries, due to certain limitations aimed at preventing battery degradation, as discussed in Vagropoulos and Bakirtzis (2013).

$$SOC_{nt}^{EV} = SOC_{n(t-1)}^{EV} + \frac{\eta_n^{EV}}{\overline{E}_n^{EV}} P_{n(t-1)}^{EV+} - \frac{1}{\eta_n^{EV} \overline{E}_n^{EV}} P_{n(t-1)}^{EV-}. \tag{20}$$

$$SOC_{nT_{dep}}^{EV} = SOC_n^{dep}. \tag{21}$$

$$\underline{SOC}_n^{arr-EV} \le SOC_{nT_{arr}}^{EV} \le \overline{SOC}_n^{arr-EV}. \tag{22}$$

As mentioned earlier, to prevent battery degradation in EVs, their charging mode transitions from constant current mode to constant voltage mode. In other words, based on a threshold SOC, called saturation SOC, their charging mode changes from constant current to constant voltage. Consequently, the maximum amount of charge/discharge power of EVs in constant current and constant voltage modes is provided by (23) (Vagropoulos and Bakirtzis, 2013).

$$\begin{cases} \overline{P}_{nt}^{EV} & \text{for} \quad 0 \le SOC_{nt}^E \le SOC_{nt}^{sat-EV} \\ \overline{P}_{nt}^{EV} \frac{1-SOC_{nt}^{EV}}{1-SOC_{nt}^{sat-EV}} & \text{for} \quad SOC_{nt}^{sat-EV} < SOC_{nt}^E \le 1 \end{cases} \tag{23}$$

As a result, the charge/discharge power of EVs in constant current and constant voltage modes is specified by (24)–(25) and (26)–(27), respectively.

$$0 \le P_{nt}^{EV+} \le a_{nt} \overline{P}_{nt}^{EV+} \psi_{nt}^{EV}. \tag{24}$$

$$0 \le P_{nt}^{EV-} \le a_{nt} \eta_n^{EV} \overline{P}_{nt}^{EV-} (1 - \psi_{nt}^{EV}). \tag{25}$$

$$0 \le P_{nt}^{EV+} \le a_{nt} \overline{P}_{nt}^{EV+} \left(\frac{1 - SOC_{nt}^{EV}}{1 - SOC_{nt}^{sat-EV}} \right) \psi_{nt}^{EV}. \tag{26}$$

$$0 \le P_{nt}^{EV-} \le a_{nt} \eta_n^{EV} \overline{P}_{nt}^{EV-} \left(\frac{1 - SOC_{nt}^{EV}}{1 - SOC_{nt}^{sat-EV}} \right) (1 - \psi_{nt}^{EV}). \tag{27}$$

As observed, all the aforementioned equations are linear except (26) and (27). To improve computational efficiency, these equations are linearized using approximation methods, as described in Gholami and Aminifar (2015). Both (26) and (27), contain the nonlinear term $SOC_{nt}^{EV} \psi_{nt}^{EV}$. According to Gholami and Aminifar (2015), this nonlinear term is replaced with a new variable (i.e. $\mathfrak{F}_{nt}^{EV} \approx SOC_{nt}^{EV} \psi_{nt}^{EV}$) and two new inequality constraints related to the newly introduced variable are added as follows:

$$-M_1 \psi_{nt}^{EV} \le \mathfrak{F}_{nt}^{EV} \le M_1 \psi_{nt}^{EV} \tag{28}$$

$$-M_1 (1 - \psi_{nt}^{EV}) \le \mathfrak{F}_{nt}^{EV} - SOC_{nt}^{EV} \le M_1 (1 - \psi_{nt}^{EV}) \tag{29}$$

2.1.3. W&S constraints

The W&S constraints encompass real-time operation equations for all EC components, including generation units, transmission lines, loads, and DERs as well as physical limitations and AC power flow equations. The active and reactive power balance equations for the EC are represented by (30) and (31), respectively.

$$\sum_{r=1}^{N_{bus}} fl_{(n,r)t\omega}^P - \kappa_n p_{t\omega}^{W\&S} = p_{nt\omega}^G + p_{nt\omega}^W - p_{nt\omega}^L + p_{nt\omega}^{Shed} - (p_{nt\omega}^{E+} - p_{nt\omega}^{E-}) - (p_{nt\omega}^{EV+} - p_{nt\omega}^{EV-}), \tag{30}$$

$$\sum_{r=1}^{N_{bus}} fl_{(n,r)t\omega}^Q = q_{nt\omega}^G - q_{nt\omega}^L + q_{nt\omega}^{Shed} + Q_n^C (\gamma_{n,t,w}^C / \overline{\gamma}_n^C), \tag{31}$$

where

$$\kappa_n = \begin{cases} 1 & \text{for} \quad n = PCC \\ 0 & \text{for} \quad n \ne PCC \end{cases} \tag{32}$$

To ensure the minimization of lost load and enhance resilience, the AC OPF is used in this paper (Cagnano et al., 2020). Therefore, according to the AC OPF formulation, the active and reactive line flows at each hour are calculated by (33) and (34), respectively.

$$fl_{(n,r)t\omega}^P = G_{(n,r)} \left(V_{nt\omega}^2 - V_{nt\omega} V_{rt\omega} cos(\theta_{nt\omega} - \theta_{rt\omega}) \right) - B_{(n,r)} \left(V_{nt\omega} V_{rt\omega} sin(\theta_{nt\omega} - \theta_{rt\omega}) \right) \tag{33}$$

$$fl_{(n,r)t\omega}^Q = -B_{(n,r)} \left(V_{nt\omega}^2 - V_{nt\omega} V_{rt\omega} cos(\theta_{nt\omega} - \theta_{rt\omega}) \right) - G_{(n,r)} \left(V_{nt\omega} V_{rt\omega} sin(\theta_{nt\omega} - \theta_{rt\omega}) \right) \tag{34}$$

The other EC operational constraints related to the AC OPF are represented by (35)–(44).

$$\underline{V}_n \le V_{nt\omega} \le \overline{V}_n \tag{35}$$

$$\underline{P}_n^G y_{nt\omega} \le p_{nt\omega}^G \le \overline{P}_n^G y_{nt\omega} \tag{36}$$

$$\underline{Q}_n^G y_{nt\omega} \le q_{nt\omega}^G \le \overline{Q}_n^G y_{nt\omega} \tag{37}$$

The sum of the flows in each transmission line from both directions is considered as the line loss, and it must be kept below a predefined acceptable value (Trodden et al., 2013).

$$fl_{(n,r)t\omega}^P + fl_{(r,n)t\omega}^P \le \overline{fl}_{(n,r)}^{Loss} \tag{38}$$

$$0 \le p_{nt\omega}^{shed} \le p_{nt\omega}^L \tag{39}$$

$$q^{shed}_{nt\omega} = p_{nt\omega}(\overline{Q}^{L}_{nt}/\overline{P}^{L}_{nt}) \tag{40}$$

$$p^{W\&S}_{t\omega} = p^{W\&S,buy}_{t\omega} - p^{W\&S,sell}_{t\omega} \tag{41}$$

$$0 \le p^{W\&S,buy}_{t\omega} \le \overline{P}^{W\&S,buy}_{t} z_{t\omega}\wp_{t\omega} \tag{42}$$

$$0 \le p^{W\&S,sell}_{t\omega} \le \overline{P}^{W\&S,sell}_{t} z_{t\omega}(1-\wp_{t\omega}) \tag{43}$$

$$0 \le c^{DG}_{nt\omega} = \lambda^{DG}_{nt}(y_{nt\omega} - y_{n(t-1)\omega}) \tag{44}$$

In this paper, to accurately model the load, the ZIP model is employed, which characterizes loads based on the voltage of buses, as discussed in Hajagos and Danai (1998). In fact, with the ZIP model, the EC operator has a better option to control loads by managing the voltage level of the bus, a technique known as conservation voltage regulation (CVR), as described in Quijano and Padilha-Feltrin (2019).

$$p^{L}_{ntw} = \overline{P}^{L}_{nt}\left(Z^{P}_{nt}(\frac{V_{nt\omega}}{V^{\circ}_{nt}})^2 + I^{P}_{nt}(\frac{V_{nt\omega}}{V^{\circ}_{nt}}) + P^{P}_{nt}\right) \tag{45}$$

$$q^{L}_{ntw} = \overline{Q}^{L}_{nt}\left(Z^{Q}_{nt}(\frac{V_{nt\omega}}{V^{\circ}_{nt}})^2 + I^{Q}_{nt}(\frac{V_{nt\omega}}{V^{\circ}_{nt}}) + P^{Q}_{nt}\right) \tag{46}$$

The operational constraints of the ESSs and EVs in the *W&S* stage resemble their model in the *H&N* stage, with the distinction that lowercase letters are used in the *W&S* stage, and the variables depend on the simulation scenarios. Consequently, the operational constraints of ESSs and EVs are represented by (47)–(58).

$$soc^{E}_{nt\omega} = sos^{E}_{n(t-1)\omega} + \frac{\eta^{E}_{n}}{\overline{E}^{E}_{n}} p^{E+}_{n(t-1)\omega} - \frac{1}{\eta^{E}_{n}\overline{E}^{E}_{n}} p^{E-}_{n(t-1)\omega}. \tag{47}$$

$$soc^{E}_{n(T_0)\omega} = SOC^{0}_{n}. \tag{48}$$

$$\underline{SOC}^{E}_{n} \le soc^{E}_{nt\omega} \le \overline{SOC}^{E}_{n}. \tag{49}$$

$$0 \le p^{E+}_{nt\omega} \le \overline{P}^{E+}_{nt} z_{t\omega}\beta^{E}_{nt\omega}. \tag{50}$$

$$0 \le p^{E-}_{nt\omega} \le \eta^{E}_{n}\overline{P}^{stg-}_{nt}(1-\beta^{E}_{nt\omega}). \tag{51}$$

$$soc^{EV}_{nt\omega} = soc^{ev}_{n(t-1)\omega} + \frac{\eta^{EV}_{n}}{\overline{E}^{EV}_{n}} p^{EV+}_{n(t-1)\omega} - \frac{1}{\eta^{EV}_{n}\overline{E}^{EV}_{n}} p^{EV-}_{n(t-1)\omega}. \tag{52}$$

$$soc^{EV}_{nT_{dep}\omega} = SOC^{dep}_{n}. \tag{53}$$

$$\underline{SOC}^{arr-EV}_{n} \le soc^{EV}_{nT_{arr}\omega} \le \overline{SOC}^{arr-EV}_{n}. \tag{54}$$

$$0 \le p^{EV+}_{nt\omega} \le b_{nt\omega}\overline{P}^{EV+}_{nt} z(t\omega)\beta^{EV}_{nt\omega}. \tag{55}$$

$$0 \le p^{EV-}_{nt\omega} \le b_{nt\omega}\eta^{EV}_{n}\overline{P}^{EV-}_{nt}(1-\beta^{EV}_{nt}). \tag{56}$$

$$0 \le p^{EV+}_{nt\omega} \le b_{nt\omega}\overline{P}^{EV+}_{nt}\left(\frac{1-soc^{EV}_{nt\omega}}{1-SOC^{sat-EV}_{nt}}\right)\beta^{EV}_{nt\omega}. \tag{57}$$

$$0 \le p^{EV-}_{nt\omega} \le b_{nt\omega}\eta^{EV}_{n}\overline{P}^{EV-}_{nt}\left(\frac{1-soc^{EV}_{nt\omega}}{1-SOC^{sat-EV}_{nt}}\right)(1-\beta^{EV}_{nt\omega}). \tag{58}$$

As mentioned earlier, to reduce the computational burden of the employed method, the non-linear equations i.e. (33)–(34), (45)–(46), and (57)–(58) are linearized in this paper. According to Trodden et al. (2013), Coffrin and Van Hentenryck (2014) in the piecewise approximation method, replacing term $v_n v_r y_{nr}$ with $v_n + v_r + y_{nt} - 2$ is acceptable, with a maximum absolute error of 0.0253. Similarly, v_i^2 can be replaced with $2v_i - 1$, with a maximum absolute error of 0.0025. In addition, considering that $\theta_{nr} = \theta_n - \theta_r$ is approximately equal to z_{nr} (see Trodden et al. (2013)), the line flow Eqs. (33)–(34) are substituted with (59)–(60).

$$fl^{P}_{(n,r)t\omega} = G_{(n,r)}\left(V_{nt\omega} + V_{rt\omega} + \Omega_{(n,r)t\omega} - 2\right) + B_{(n,r)}(\theta_{nt\omega} - \theta_{rt\omega}), \tag{59}$$

$$fl^{Q}_{(n,r)t\omega} = -B_{(n,r)}\left(V_{nt\omega} + V_{rt\omega} + \Omega_{(n,r)t\omega} - 2\right) + G_{(n,r)}(\theta_{nt\omega} - \theta_{rt\omega}), \tag{60}$$

where $\Omega_{(n,r)t\omega} = h^{1}_{(n,r)t\omega,i}(\theta_{nt\omega} - \theta_{rt\omega}) + h^{2}_{(n,r)t\omega,i}$ for all $(\theta_{nt\omega} - \theta_{rt\omega}) \in [x_{nr,i}, x_{nr,i+1}]$, $i = 0, 1, \ldots, I-1$. Note that, h^1 and h^2 are selected in such a way that Ω and $cos(\theta_{nt\omega} - \theta_{rt\omega})$ coincide at breakpoints x_i.

With the consideration that the voltage of EC buses is maintained close to 1, the load model can be approximated shown in (61) and (62).

$$p^{L}_{ntw} = \overline{P}^{L}_{nt}\left(Z^{P}_{nt}(1 + 2(v_{nt\omega} - v^{\circ}_{nt})) + I^{P}_{nt}(\frac{v_{nt\omega}}{v^{\circ}_{nt}}) + P^{P}_{nt}\right). \tag{61}$$

$$q^{L}_{ntw} = \overline{Q}^{L}_{nt}\left(Z^{Q}_{nt}(1 + 2(v_{nt\omega} - v^{\circ}_{nt})) + I^{Q}_{nt}(\frac{v_{nt\omega}}{v^{\circ}_{nt}}) + P^{Q}_{nt}\right). \tag{62}$$

Similar to (26) and (27), the last non-linear equations, i.e., (57) and (58), are linearized by introducing a new variable and adding two inequality constraints.

2.1.4. Coordinating constraints

In addition to *H&N* and *W&S* constraints, there are some other constraints that show the effect of the *W&S* constraints on *H&N* constraints. This set of constraints is categorized as coordinating constraints. The corrections in power exchange with the upstream network are modeled through several equality and inequality constraints, which are shown in (63)–(66).

$$\Delta p^{w\&S,B}_{t\omega} = p^{W\&S,B}_{t\omega} - P^{H\&N,B}_{t}. \tag{63}$$

$$\Delta p^{W\&S,S}_{t\omega} = p^{W\&S,S}_{t\omega} - P^{H\&N,S}_{t}. \tag{64}$$

$$\Delta p^{W\&S,B}_{t\omega} = \Delta p^{W\&S,B+}_{t\omega} - \Delta p^{W\&S,B-}_{t\omega}. \tag{65}$$

$$\Delta p^{W\&S,S}_{t\omega} = \Delta p^{W\&S,S+}_{t\omega} - \Delta p^{W\&S,S-}_{t\omega}. \tag{66}$$

Finally, the demand-side deployed reserves are modeled by the following equality and inequality equations.

$$p^{L}_{nt\omega} = P^{L}_{nt} - r^{LU}_{nt\omega} + r^{LD}_{nt\omega}. \tag{67}$$

$$0 \le r^{LU}_{nt\omega} \le R^{LU}_{nt}. \tag{68}$$

$$0 \le r^{LD}_{nt\omega} \le R^{LD}_{nt}. \tag{69}$$

2.1.5. Carbon emission (CE) constraints

The responsibility of governments in addressing global warming involves reducing the amount of carbon in the air, as this is one of the most effective strategies against climate change. Therefore, the electrical energy sector is transitioning towards net-zero carbon systems. In this paper, the energy injected from carbon-based resources, such as DGs and the main grid, is limited in accordance with carbon emission considerations. These constraints are incorporated into both the *H&N* and *W&S* stages. The *H&N* constraints related to carbon emissions are provided in (70)–(73).

$$CE^{H\&N,up}_{t} = P^{H\&N,b}_{t} CI^{up}_{t}. \tag{70}$$

$$0 \le CE^{H\&N,up}_{t} \le \overline{CE}^{up}_{t}. \tag{71}$$

$$CE^{H\&N,G}_{t} = \sum_{n=1}^{N_{bus}} P^{G}_{nt} CI^{G}_{nt}. \tag{72}$$

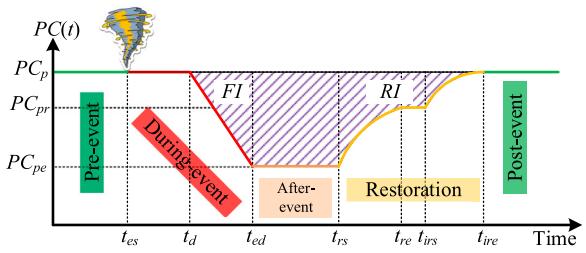

Fig. 1. The general time frame of the performance of an energy community facing an extreme event.

$$0 \le CE_t^{H\&N,G} \le \overline{CE}_t^{G}. \tag{73}$$

Similarly, the W&S carbon emission constraints, which pertain to the imported power from the main grid and DG generation, are as follows:

$$ce_{t\omega}^{W\&S,up} = p_{t\omega}^{W\&S,b} CI_t^{up}. \tag{74}$$

$$0 \le ce_{t\omega}^{W\&S,up} \le \overline{CE}_t^{up}. \tag{75}$$

$$ce_{t\omega}^{W\&S,G} = \sum_{\omega=1}^{N_\Gamma} \nu_\omega \sum_{n=1}^{N_{bus}} p_{nt\omega}^{G} CI_{nt}^{G}. \tag{76}$$

$$0 \le ce_{t\omega}^{W\&S,G} \le \overline{CE}_t^{G}. \tag{77}$$

2.1.6. Resilience objective function

Achieving an accurate assessment of the resilience level of an EC requires defining proper resilience metrics that consider event characteristics as well as system performance during the event. In this paper, four resilience metrics are considered, including the fragility index (FI), the restoration index (RI), the voltage deviation index (VDI), and the lost energy index (LEI). The FI and RI metrics indicate the withstanding ability and restoration efficiency of the system against the event and are calculated using the EC performance curve during the event. The VDI and LEI metrics represent the quality of the EC during the event and are obtained by the optimal power flow calculations. According to Fig. 1, the time frame of the performance of an EC is divided into five phases, namely pre-event, during-event, after-event, restoration, and post-event (Younesi et al., 2022b). The performance curve can be calculated based on different parameters of the power system, such as the percentage of operational components or the percentage of supplied loads during the event (Younesi et al., 2022a). In this paper, the percentage of the supplied load is used to calculate the EC performance curve as follows:

$$PC_{t\omega} = \left(1 - \sum_{n=1}^{N_{bus}} \frac{p_{nt\omega}^{shed}}{P_{nt}^{L}}\right) \times 100. \tag{78}$$

In Fig. 1, the time durations between event phases have a large influence on the calculated resilience metrics and exactly determining these time periods is difficult, because they depend on the event severity, the amount of the damages, and the recovery facilities and efficiency. In this paper, it is assumed the degradation will start immediately after the event(i.e., $(t_d - t_{es}) = 0$). In addition, the degradation will continue at a fixed rate until the end of the event which is acquired randomly in scenarios. It is also assumed the recovery immediately starts after the event (i.e., $(t_{rs} - t_{ed}) = 0$) and will continue at a fixed rate. In other words, all of these time durations are assumed to be relevant to the event duration which is a stochastic parameter and determined through scenarios.

Based on the performance curve shown in Fig. 1, the EC resilience is represented in the dashed area, which should be minimized to achieve a more resilient EC. Assume the Γ as the set of scenarios. Therefore, $N_\Gamma = |\Gamma|$ represents the number of scenarios. In addition, the probability of each scenario is donated by ν_ω, which $\omega \in \Gamma$. Referring to the area depicted for the FI index in Fig. 1, it can be calculated using (79).

$$FI = \sum_{\omega=1}^{N_\Gamma} \nu_\omega \left\{ \frac{\int_{t_{d,\omega}}^{t_{pe,\omega}} \left[PC_{p,\omega} - PC_\omega(t)\right] dt}{PC_{p,\omega}(t_{pe,\omega} - t_{d,\omega})} \right\}. \tag{79}$$

To ensure the simulation remains tractable, the FI index can be approximated based on the area of a triangle, as demonstrated in Fig. 1, and is given as follows:

$$FI \approx \widehat{FI} = \sum_{\omega=1}^{N_\Gamma} \nu_\omega \left[\frac{\left(PC_{p,\omega} - PC_{pe,\omega}\right)\left(t_{pe,\omega} - t_{d,\omega}\right)}{2PC_{p,\omega}(t_{pe,\omega} - t_{d,\omega})} \right]. \tag{80}$$

Referring to Fig. 1, the time period from t_{rs} to t_{ire} is associated with the restoration efficiency and is calculated as the RI index using (81).

$$RI = \sum_{\omega=1}^{N_\Gamma} \nu_\omega \int_{t_{rs,\omega}}^{t_{ire,\omega}} \frac{PC_{p\omega} - PC_\omega(t)}{(PC_{p,\omega} - PC_{pe,\omega})(t_{ire,\omega} - t_{rs,\omega})} dt. \tag{81}$$

Analogous to (80), the RI index can be approximated based on the area of the dashed regions within the interval $t \in [t_{rs},\ t_{ire}]$ as expressed by (82).

$$\begin{aligned} RI \approx \widehat{RI} = \sum_{\omega=1}^{N_\Gamma} \nu_\omega \Bigg[& \frac{(PC_{p,\omega} - PC_{pr,\omega})(t_{irs,\omega} - t_{rs,\omega})}{(PC_{p,\omega} - PC_{pe,\omega})(t_{ire,\omega} - t_{rs,\omega})} \\ & + \frac{(PC_{pr,\omega} - PC_{pe,\omega})(t_{re,\omega} - t_{rs,\omega})}{2(PC_{p,\omega} - PC_{pe,\omega})(t_{ire,\omega} - t_{rs,\omega})} \\ & + \frac{(PC_{p,\omega} - PC_{pr,\omega})(t_{ire,\omega} - t_{irs,\omega})}{2(PC_{p,\omega} - PC_{pe,\omega})(t_{ire,\omega} - t_{rs,\omega})} \Bigg]. \end{aligned} \tag{82}$$

It is important to note that the dashed area between t_{ed} and t_{rs}, considered as the time required for preparing the restoration process, depends on the damages to other infrastructure such as transportation and communications, redundancy of DERs, and the availability of mobile resources and transformers. In this paper, it is assumed that portable resources become available immediately following the event. As a result, the FI and RI metrics are the sole metrics that need to be optimized in order to improve resilience.

The remaining two resilience metrics, VDI, and LEI, indicate the merit of the EC operation during emergencies following an extreme event. They are calculated based on real-time variables derived from the optimal power flow (OPF). The VDI metric is computed as a function of the voltage deviation from the scheduled value for each bus, $|V_n^\star|\ \forall\ n = 1, \ldots, N_{bus}$, as follows, according to:

$$VDI = \sum_{n=1}^{N_{bus}} \left\{ \sum_{\omega=1}^{N_\Gamma} \nu_\omega \left[\sum_{t=1}^{T} \left(|V_{n\omega}^\star| - |V_{nt\omega}| \right) \right] \right\}. \tag{83}$$

The LEI index is determined by the percentage of lost energy in the proposed scheduling time horizon, as described as follows:

$$LEI = \sum_{n=1}^{N_{bus}} \left\{ \sum_{\omega=1}^{N_\Gamma} \nu_\omega \left[\sum_{t=1}^{T} \left(\frac{P_{nt\omega}^{shed} \Delta t}{p_{nt\omega}^{l} T} \right) \right] \right\}. \tag{84}$$

As evident from (80), (82), and (83)–(84), the defined metrics for resilience are dimensionless and obtained per unit. This allows for the consideration of an appropriate resilience function that combines these metrics to ultimately assess the overall resilience score of the EC. Given that for a resilient EC, all defined metrics for resilience should be close to zero, a sum function is employed in this paper to map the resilience metrics into the overall EC resilience score and, consequently, the resilience objective function (f_2) as follows:

$$f_2 = FI + REI + VDI + LEI. \tag{85}$$

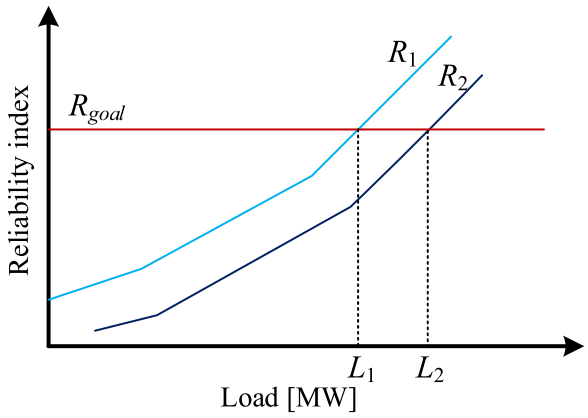

Fig. 2. The reliability after adding new DER units.

2.2. ELCC

The increasing penetration level of renewable and dispatchable DERs in modern ECs has made DER-based ELCC more critical for EC planners and operators. Particularly, the capacity credit of DERs can be utilized for enhancing the fast restoration of EC after an extreme event and ensuring the resilient operation of EC. In other words, the DER-based ELCC provides a means to assess the capacity value of a set of DER sources and serves as a measure of additional load that the system can supply with no change in reliability (Garver, 1966). Thus, it can be defined based on reliability metrics such as loss of load probability (LOLP), and loss of load expectation (LOLE), among others. A simple illustration of the proposed method for calculating ELCC in this paper based on the reliability metric, is shown in Fig. 2.

In Fig. 2, R_1 and R_2 represent the reliability index of the EC before and after adding new DER units, respectively, while R_{goal} denotes the target reliability index. As shown in Fig. 2, the ELCC is calculated as follows:

$$ELCC_{\%}^{DER} = \left(\frac{L_2 - L_1}{\text{Load}_{\text{total}}}\right) \times 100. \tag{86}$$

In this paper, the LOLP index is calculated in both stages using (87) and (88). The $LOLP^{H\&N}$ is calculated in day-ahead calculations and represents the expected LOLP of the system. Additionally, $lolp^{W\&S}$ is determined dynamically based on the generated scenarios, which take into account the event characteristics.

$$LOLP^{H\&N} = \frac{1}{N_t}\sum_{t=t_0}^{N_t}\zeta_t, \tag{87}$$

$$lolp^{W\&S} = \frac{1}{N_\Gamma}\sum_{\omega=1}^{N_\Gamma} v_\omega P_{e,\omega}\frac{1}{N_t}\sum_{t=t_0}^{N_t}\zeta_{t\omega}, \tag{88}$$

where $\zeta_{t\omega}$ is a binary variable and is 1 if at time t in the scenario ω the shedded load becomes greater than zero (i.e. $\sum_n^{N_{bus}} p_{nt\omega}^{shed} > 0$). Otherwise (i.e. $\sum_n^{N_{bus}} p_{nt\omega}^{shed} = 0$), it is 0. Note that $p_{nt\omega}^{shed}$ is a positive variable initially set to zero.

In fact, the LOLE index is another expression of LOLP, which is defined based on minutes, hours, and days per scheduling horizon. In this paper, LOLE is defined based on minutes per day, and for both stages, it is given as follows:

$$LOLE^{H\&N} = LOLP^{H\&N} \times 24 \times 60 \quad \text{minutes/day}. \tag{89}$$

$$lole^{W\&S} = lolp^{W\&S} \times 24 \times 60 \quad \text{minutes/day}. \tag{90}$$

In this paper, LOLE is employed to calculate the ELCC for each stage. The ELCC calculation procedure is illustrated in Fig. 3.

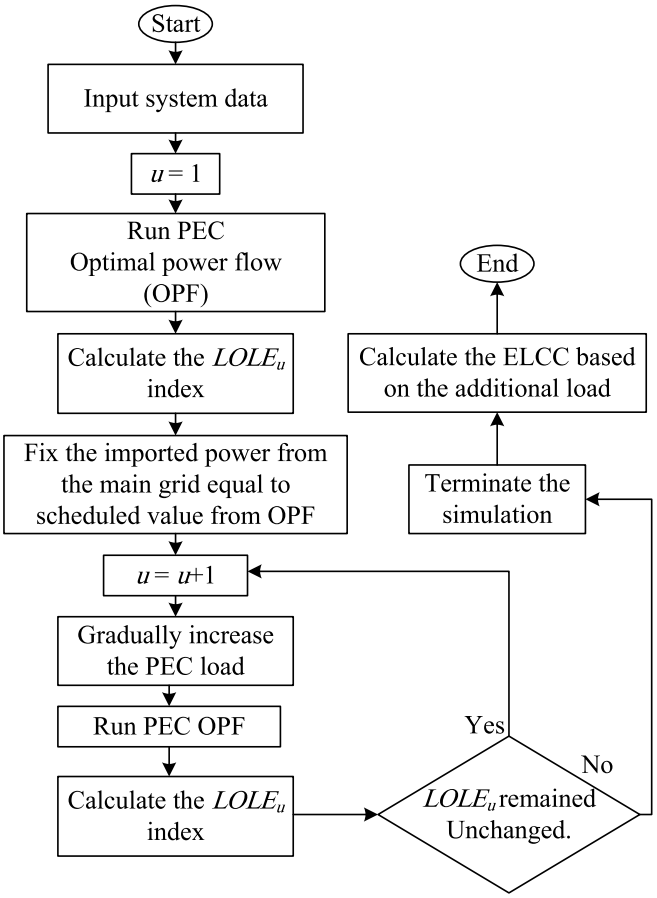

Fig. 3. The flowchart of calculating the ELCC.

As depicted in Fig. 3, the imported power from the main grid remains fixed at the value obtained from the OPF. Therefore, the power of DERs is utilized to supply the additional load. Ultimately, the LOLE is employed to determine the ELCC of DER units within the EC.

2.3. Integrating the ELCC into the general TSERS

After computing the ELCC in both stages as described in the previous section, it is integrated into the proposed resilience-economic EC two-stage scheduling formulation for both stages. To incorporate ELCC into the formulations, two new inequality constraints are added, as presented in (91) and (92) for the *H&N* and *W&S* stages, respectively.

$$\underline{ELCC} \le ELCC^{H\&N} \le \overline{ELCC}. \tag{91}$$

$$\underline{ELCC} \le elcc^{W\&S} \le \overline{ELCC}. \tag{92}$$

2.4. Mesh-view and disaster characteristics

The mesh view is a method for determining the precise location of system components and modeling the behavior of extreme events on the system (Younesi et al., 2022c). In this method, the EC is divided into a finite number of two-dimensional cells. Each cell is described by a pair of integers (e.g., (x,y)). By using the mesh view, the accurate location of the EC components and the extreme event characteristics such as the starting point (cell), route, endpoint, and the interaction of the event with the EC components can be determined. Taking this

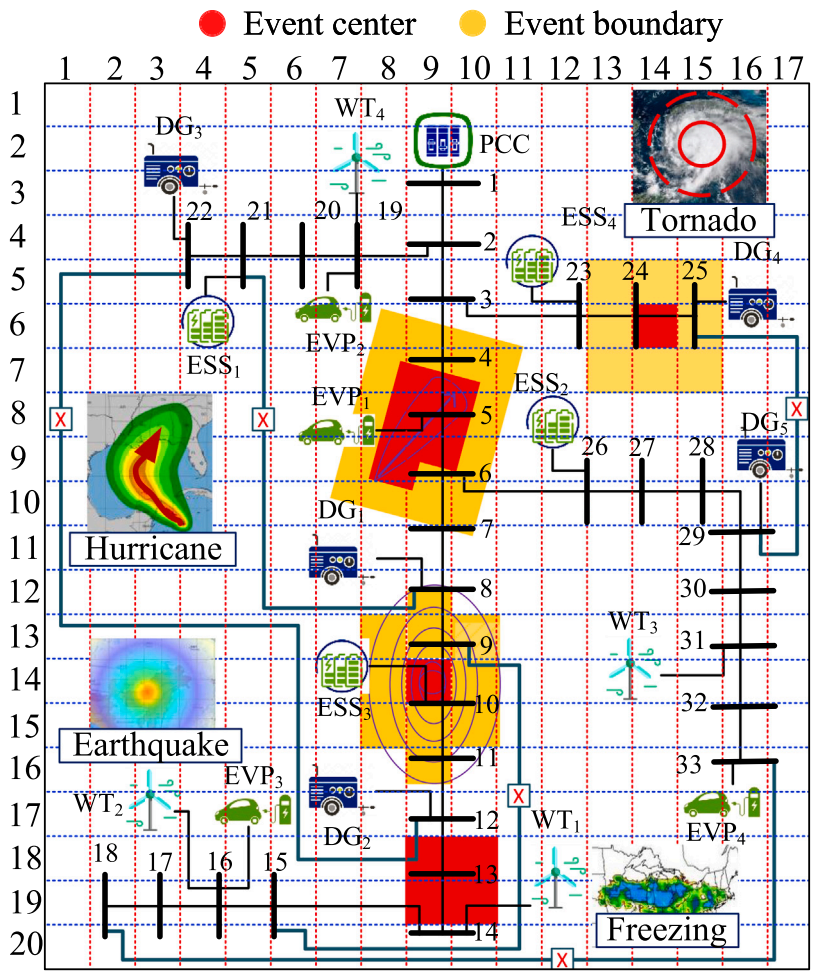

Fig. 4. The mesh-view of a sample EC considering various events behavior.

information into account, the damage assessment of the EC following an extreme event can be achieved with higher accuracy. Fig. 4 displays an example of the mesh view of an EC, considering the behavior of different types of events.

In this paper, the resilience of the EC is assessed by considering four event types: hurricanes, tornadoes, earthquakes, and ice freezing. The behavior of each event on the mesh-view is inspired by their natural performance, as depicted in Fig. 4, the red cells represent the event center, indicating that the equipment located in these cells will be significantly affected. The light-orange cells represent the event boundaries, and equipment in these cells has a high probability of being affected. The remaining equipment outside of the event center and boundaries is assumed to remain operational. For instance, in the case of a tornado in Fig. 4, bus 24 and line 24–25 are heavily affected. Additionally, buses 24 and 25, as well as line 23–24, have a high probability of being affected.

2.5. The proposed optimization model

Eventually, after obtaining the mathematical model of different EC operation players such as DERs, Loads as well as carbon emission and ELCC-related constraints, the final optimization problem is formulated as follows:

$$\begin{aligned}
&\min \quad \{f_1, f_2, f_3\} \\
&\text{s.t.} \\
&\qquad H\&N \text{ and } W\&S \text{ constraints}: \\
&OPF \quad ((6)\text{–}(14)) \text{ and } ((30)\text{–}(46)), \\
&ESSs \quad ((15)\text{–}(19)) \text{ and } ((47)\text{–}(51)), \\
&EVPs \quad ((20)\text{–}(27)) \text{ and } ((52)\text{–}(58)), \\
&CE \quad ((70)\text{–}(73)) \text{ and } ((74)\text{–}(77)), \\
&ELCC \quad (91) \text{ and } (92), \\
&\qquad Coordinating \text{ constraints}: \\
&\qquad ((63)\text{–}(69)).
\end{aligned} \tag{93}$$

2.6. The Augmented ε-constraint method for multi-objective optimization

In order to deal with trade between cost, resilience, and emission in the proposed tri-objective optimization problem, the augmented ε-constrained method is used in this paper. The general formulation of the augmented ε-constrained method is given as (Zakariazadeh et al., 2014):

$$\begin{aligned}
&\min \quad \left(f_1 - \delta \sum_{k=2}^{K} \frac{s_k}{r_k}\right) \\
&\text{s.t.} \\
&\qquad f_k + s_k - e_k^z \quad k = 2, \ldots, K;\ s_k \in R^+
\end{aligned} \tag{94}$$

where

$$e_k^z = f_k^{\max} - \frac{f_k^{\max} - f_k^{\min}}{q_k - 1} \times z, \quad z = 0, 1, \ldots, q_k. \tag{95}$$

where s_k is slack variable, δ is a scaling factor, $f_k^{\max}$ and $f_k^{\max}$ are the maximum and minimum of the kth objective function, respectively. e_k^z is the zth range of the kth objective function, r_k is the range of the kth

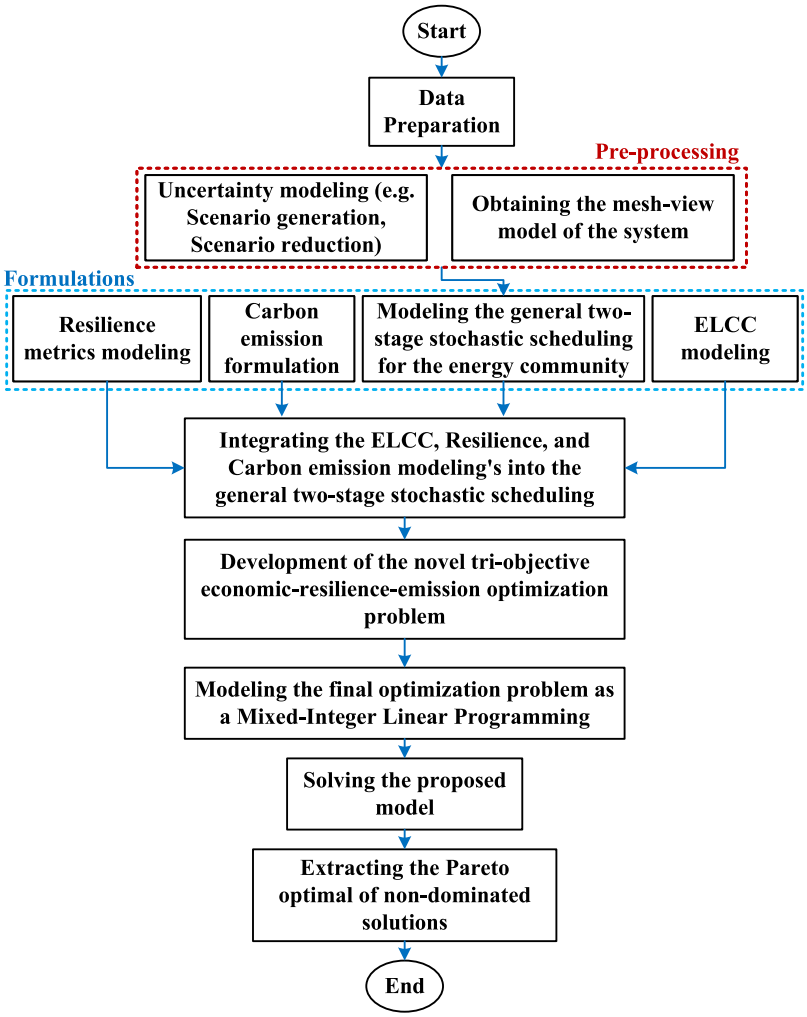

Fig. 5. The flowchart of the proposed tri-objective economic-resilience-emission optimization problem modeling.

objective function (i.e., $f_k^{\max} - f_k^{\min}$), and q_k is the number of equal part.

The maximum and minimum of each objective function ($f_k^{\min}$ and $f_k^{\min}$) are obtained from the individual optimization of each objective function. Then one of the objective functions is considered as the master (f_1) and the ranges of each k-1 objective function are considered as the new constraints and the Pareto front of the non-dominated solutions are achieved. It should be noted that in this paper, the resilience objective function is considered as the master, and cost and emission objectives are considered as the constraints. The flowchart of the proposed methodology is shown in Fig. 5. According to Fig. 5, the input data will be used in the pre-processing stage. Then the formulations will be conducted and the final tri-objective economic-resilience-emission optimization problem is modeled as a mixed-integer linear programming. Finally, the proposed model is solved and the Pareto front of non-dominated solutions is extracted that can be used for informed decision-making based on the DSO limitations and priorities.

3. Simulation results

3.1. Scenario generation

In this paper, scenarios are generated based on uncertain parameters, as illustrated in Fig. 6. The uncertain parameters, including the probability of event occurrence, event type, event severity level, event location, market price, and WT generation, are initially classified. The uniform distribution function is then employed to generate 5000 scenarios based on these uncertain parameters. To alleviate the computational burden of simulations, the number of scenarios is subsequently reduced to 10 using the *K-mean* clustering method (Younesi et al., 2021a).

To evaluate the effectiveness of the proposed scheduling method the results are compared to the methodology presented in Younesi et al. (2022b) considering three case studies namely Case I, Case II, and Case III. It is worth noting that, cases I and II are taken from Younesi et al. (2022b) with some minor modifications. Each case study prioritizes different objectives as follows:

- Case I: In this case, the economic index of the energy community is the sole objective function, while the resilience and carbon emission indices are ignored.
- Case II: In this case, only the resilience index is considered as the objective.
- Case III: In this case, all three indices are considered using the augmented ε-constraint method.

These case studies are selected based on prioritizing each objective function. In other words, the simulations present the impact of integrating each objective function (i.e. economic, resilience, and carbon

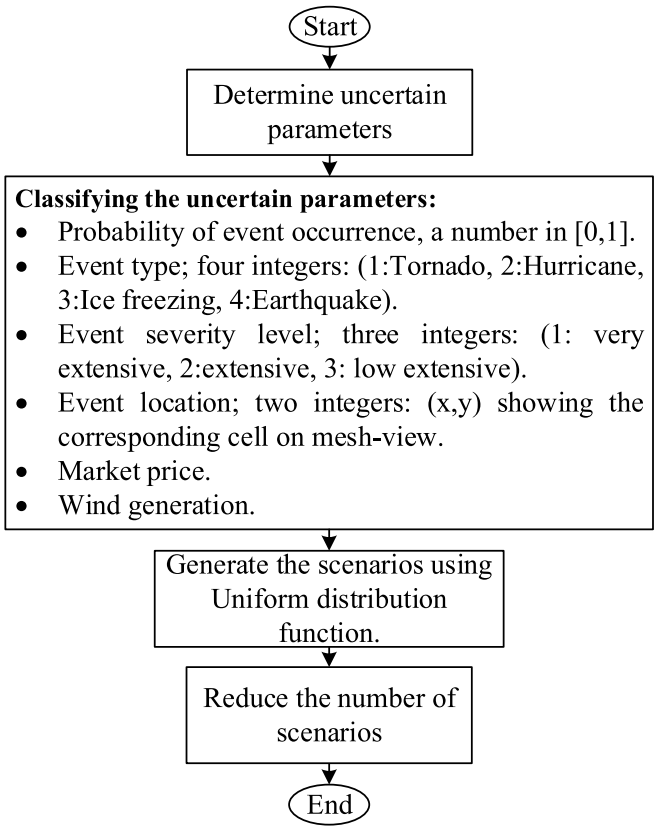

Fig. 6. The scenario generation procedure.

emission) in the final optimization problem to highlight the role of DERs and their ELCC. In fact, the decision-maker can investigate the impact of each objective function on the simulations and then will be able to make informed decisions on system planning considering their priorities and system limitations comparing the results in different case studies. It is worth noting that the system planner has the flexibility to assign different constraints to each resilience metric based on its planning priorities and constraints, therefore the "best optimal solution" has been identified in the Pareto front by fixing some constraints to the three metrics. In this paper, the Pareto front of non-dominated solutions is obtained, one of the solutions has been selected, and the operator can adjust the solution according to its priorities. The proposed methodology was formulated using GAMS and solved on a device with a Core i7 processor and 16 GB RAM.

3.2. Case study 1: IEEE 33-bus test system

This system consists of 33 buses, 33 lines, 5 distributed diesel generators, 4 energy storage devices, 4 electric vehicle parking (EVP) lots, and 4 wind generators. The technical data of the system and its components can be found in the Ref. (Younesi et al., 2021a). The allocation of the distributed generation units is assumed to be as shown in Fig. 4 (Younesi et al., 2021a). Due to physical and geographical limitations such as distance, mountains, and lakes, it is not possible to add maneuvering lines between all system buses. However, in this paper, it is assumed that 5 new lines are available to be added in the reconfiguration plan, taking into account these limitations. These new possible lines are highlighted in blue in Fig. 4 and they are initially disconnected (off) in normal operating conditions. The new possible lines are represented by the dark blue color in Fig. 4 and they are initially off (disconnected) in normal condition. Simulations are conducted in all three cases based on the stochastic scenarios.

The optimal reconfiguration plans for different cases are illustrated in Fig. 7. It is observed that in Case I, based on the economic index, three new lines need to be added between buses (8,21), (18,33), and (25,29). However, in Cases II and III, only two new lines between buses (8,21) and (18,33) are required. This indicates that line (25,29) primarily contributes to the economic index and does not significantly improve the resilience and carbon emission indices. On the other hand, lines (8,21) and (18,33) are crucial as they have a positive impact on all three indices, namely economic, resilience, and carbon emissions.

The carbon emissions from the distributed generation units are assumed to be fixed at 190 g/kWh throughout the 24 h of the day. However, the carbon emissions from the main grid vary during different hours of the day. The carbon intensity data for a typical autumn day are collected from the official carbon intensity API for Great Britain developed by National Grid (available at https://carbonintensity.org.uk/) and are depicted in Fig. 8. This data provides information about the carbon intensity levels during different hours, allowing for more accurate modeling and analysis of the carbon emissions from the main grid.

Fig. 9 illustrates the carbon intensity of the distributed generation (DG) units and the main grid in different cases. It is important to note that, for the purpose of assessing the results, scenario 4 has been randomly selected as an example. In scenario 4, a very severe hurricane event has occurred, starting at 9:00 PM (hour 21:00) from cell (20, 3) and ending at 5:00 AM the following day in cell (2, 6). This event has significantly impacted the entire system, affecting multiple system components. The carbon intensity data provide insights into the variations in carbon emissions from both DG and the main grid during this extreme event scenario.

Based on Fig. 9(a), the following observations can be made regarding the carbon intensity in different cases:

- In Case I, the carbon intensity of the distributed generation (DG) units is higher during the hours of 3:00 PM to 7:00 PM. This is due to the high market prices during these hours, leading to increased utilization of DGs to minimize energy purchases from the main grid and reduce costs;
- In Case II, where only the resilience index is considered, the carbon intensity of DGs is notably higher compared to the other cases. In this case, the primary focus is on improving resilience, while the cost and carbon intensity indices are disregarded;
- In Case III, where the carbon intensity is incorporated in the objective function, it can be observed that the carbon emissions are significantly reduced compared to the other cases. This indicates that considering the carbon intensity in the optimization process leads to a notable decrease in carbon pollution.

Regarding the grid carbon intensity shown in Fig. 9(b), it is observed that during the hours of 9:00 PM to 5:00 AM, the carbon intensity is zero. This is because, during this time period, the energy community is dealing with extreme events and relies minimally on imports from the main grid. Similar to Fig. 9(a), the carbon intensity is highest in Case II and lowest in Case III, highlighting the impact of incorporating carbon intensity in the objective function.

The concept of ELCC in this paper is used to assess the capacity value of DG and wind units in enhancing the resilience of the energy community. The ELCC represents the reliable extra power that DG and wind units can provide during an emergency event, contributing to the improvement of resilience. It should be noted that the ELCC is calculated based on the OPF, which is based on the EC topology. Therefore, it can be concluded that the impacts of the newly added line in the reconfiguration plan are considered in the ELCC calculation, inherently. Fig. 10 illustrates the calculated ELCC of DG and wind units in the simulation cases. It is observed that in Case I, where the resilience index is ignored, the generation of DGs and wind turbines decreases during the event hours (21:00 PM to 5:00 AM). Consequently, their

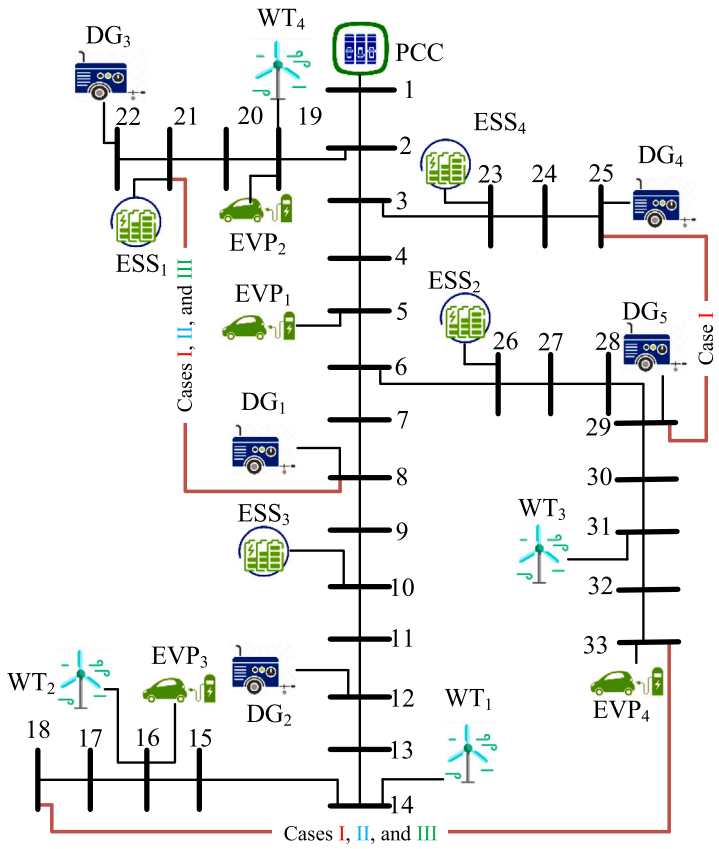

Fig. 7. The proposed energy community reconfiguration results.

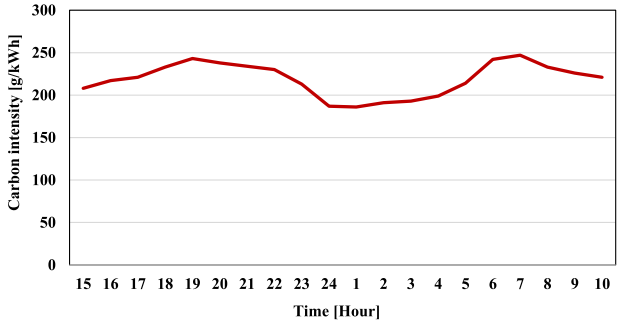

Fig. 8. The carbon intensity data of the main grid for the proposed scheduling day.

ELCC increases, indicating their potential to provide additional reliable power during the event. It is important to note that the maximum ELCC level is not limited and can reach up to 100%, while the lower limit is set to 20% in all case studies. From a resilience perspective, in Cases II and III, where the resilience index is considered, the ELCC of DG and wind units decreases compared to Case I. This implies that the energy community operator utilizes these units at their full capacity to improve the resilience index. As a result, the ELCC decreases, signifying the enhanced capability of these units to provide reliable power during the event. In fact, the analysis of the ELCC values reveals that the integration of the resilience index in the optimization process (Cases II and III) leads to a decrease in the ELCC of DG and wind units. This indicates a stronger reliance on these units to enhance the resilience of the energy community during an emergency event.

The Pareto front of non-dominated solutions for the proposed three objective optimization problems is displayed in Fig. 11. In this paper, the resilience objective function is considered the master objective, and thus, the Pareto front showcases the trade-off between the resilience objective function and each of the other objectives (i.e. operating cost, carbon emission, and both of them). The presented Pareto front provides a comprehensive visualization of the trade-off between different objectives, allowing decision-makers to make informed decisions based on their specific requirements and preferences (see Harrison et al. (2007), Zakariazadeh et al. (2014) for more detail).

In fact, the decision maker can have measures of the consequences of its choices in terms of all economic-resilience-emission objective functions and then select the best solution considering the regulatory limits related to economic constraints, resilience-oriented performance, and emission constraints related to the energy community. It should be noted that the selection of the best solution is not the main concern of this paper, therefore, it is assumed that the EC operator as the decision-maker determine the upper admissible levels allowed for each economic, carbon emission, and resilience objective function and then select the best solution among the non-dominated solutions in the Pareto front, which is located in the acceptable range for all objective functions. In this paper, it is assumed that the EC operator selects the best solution from the non-dominated solutions from the Pareto front by fixing the following constraints to the three metrics as follows: $f_1 < 15473.18778\$$, $f_2 < 5.506$, and $f_3 < 55.80Kg$. It is worth noting that the selected solution is just used for analysis purposes while the final decision is made by the decision maker, not by the analyst.

The performance curve of the energy community, depicted in Fig. 12, and the resilience metrics, shown in Fig. 13, serve to showcase the effectiveness of the proposed multi-objective scheduling scheme

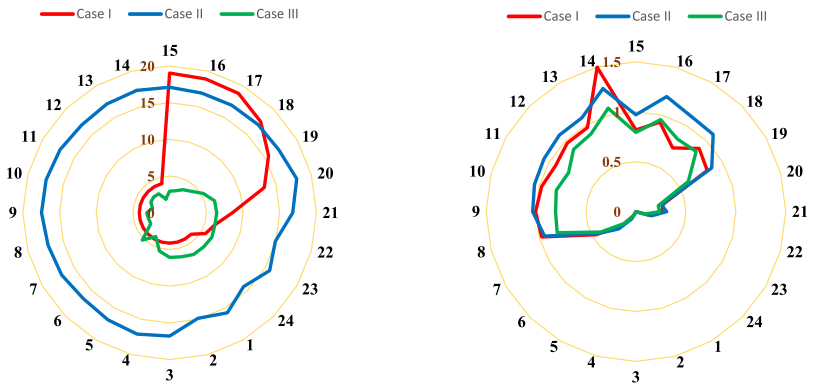

Fig. 9. The carbon emission of DG and grid in different case studies.

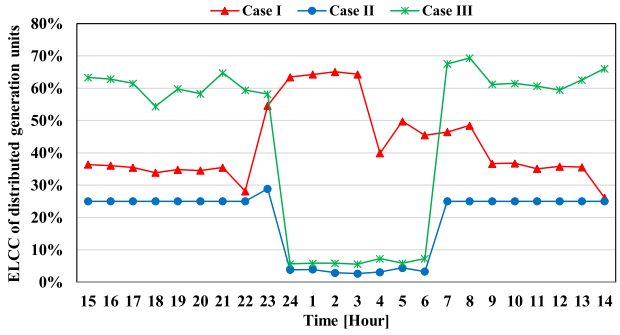

Fig. 10. The ELCC of distributed generation units in scenario 4.

in enhancing resilience. It is evident from the figures that Case I, which does not prioritize resilience as an objective, yields the worst performance curve. Conversely, Case II, which focuses solely on resilience, exhibits the best performance curve. These results highlight the importance of incorporating resilience as a key objective in the scheduling process. By considering resilience alongside other objectives, the system's ability to withstand and recover from extreme events can be significantly improved. This demonstrates the value of a comprehensive and balanced approach that takes into account both economic considerations and the system's ability to adapt and respond to disturbances. The performance curve provides a visual representation of how different scheduling strategies impact the overall performance of the energy community during extreme events. It serves as a valuable tool for decision-makers to assess and compare the effectiveness of different scheduling approaches in terms of their impact on system resilience.

Fig. 13 depicts the variations of individual resilience metrics and the overall energy community resilience index in different case studies. The overall resilience index is computed as the sum of the four resilience metrics (FI, RI, VDI, and LEI) with equal weight factors of 1, as indicated in Eq. (85). It is worth noting that the system planner has the flexibility to assign different weight factors to each resilience metric, based on their planning priorities. By adjusting the weight factors, the planner can allocate more or less importance to specific resilience metrics, thereby tailoring the overall resilience index to align with the specific goals and requirements of the energy community.

Fig. 14 illustrates the revenue of the energy community in scenario 4 for different case studies. It can be observed that in case II, where the focus is solely on resilience, the revenue decreases compared to case I. This reduction in revenue is attributed to the allocation of resources and generation capacity to enhance the system's resilience during the event. On the other hand, in case III, where a balanced integration of economic, resilience, and carbon indices is considered, the revenue during normal operation hours can surpass that of case I. However, during the event (i.e., hours 24:00 AM to 3:00 AM), the revenue in case III is lower than that in case I due to the prioritization of resilience and carbon emission reduction over maximizing economic gains. Overall, the results highlight the trade-offs between economic performance, resilience enhancement, and carbon emission reduction in different operational scenarios.

To demonstrate the behavior of EVPs and ESS devices, the performance of the EVP located at bus 33, and ESS located at bus 26 during scenario 4 are shown in Fig. 15.

From Fig. 15(a), it can be observed that the EV joined the EC at 20:00 PM and disconnected from the system at 10:00 AM. Throughout its connection period, the EV was charged during normal operation hours and when the energy price was low. It is important to note that during the event, which occurred between 21:00 PM to 5:00 AM, the EV was not allowed to charge, but it discharged based on its SOC to support the power supply in islanding mode. Similarly, the Energy Storage System (ESS) discharged during the event to help mitigate load losses. Additionally, the ESS was charged during hours when the market price was low and discharged during hours when the market price was high, such as at 17:00 PM. In essence, Fig. 15 demonstrates that both the EVP and the ESS devices contribute to enhancing grid resilience while keeping operating costs low.

Fig. 16 illustrates the total wind generation in scenario 4. It is observed that the resilience index in cases II and III has resulted in an increase in the overall wind generation. However, during the event hours, the wind generation decreases. This decrease can be attributed to the impact of the event on the distribution lines, which reduces their capacity to transfer power within the system. As a result, the wind generation during these hours is adversely affected. Therefore, the resilience measures implemented in cases II and III have positively influenced the total wind generation, except during the event hours when the distribution lines' power transfer capacity is compromised, leading to a decrease in wind generation.

Fig. 17 provides insights into the performance of the Distributed Generation (DG) units and the amount of imported power from the main grid in scenario 4. It allows for a deeper investigation into the relationship between DG generation and imported power. During the event period (hours 21:00 PM to 6:00 AM), the energy community operates in islanding mode, meaning that no power is imported from the main grid. Consequently, the imported power is zero during this period. In case III, where carbon emissions are taken into account, both

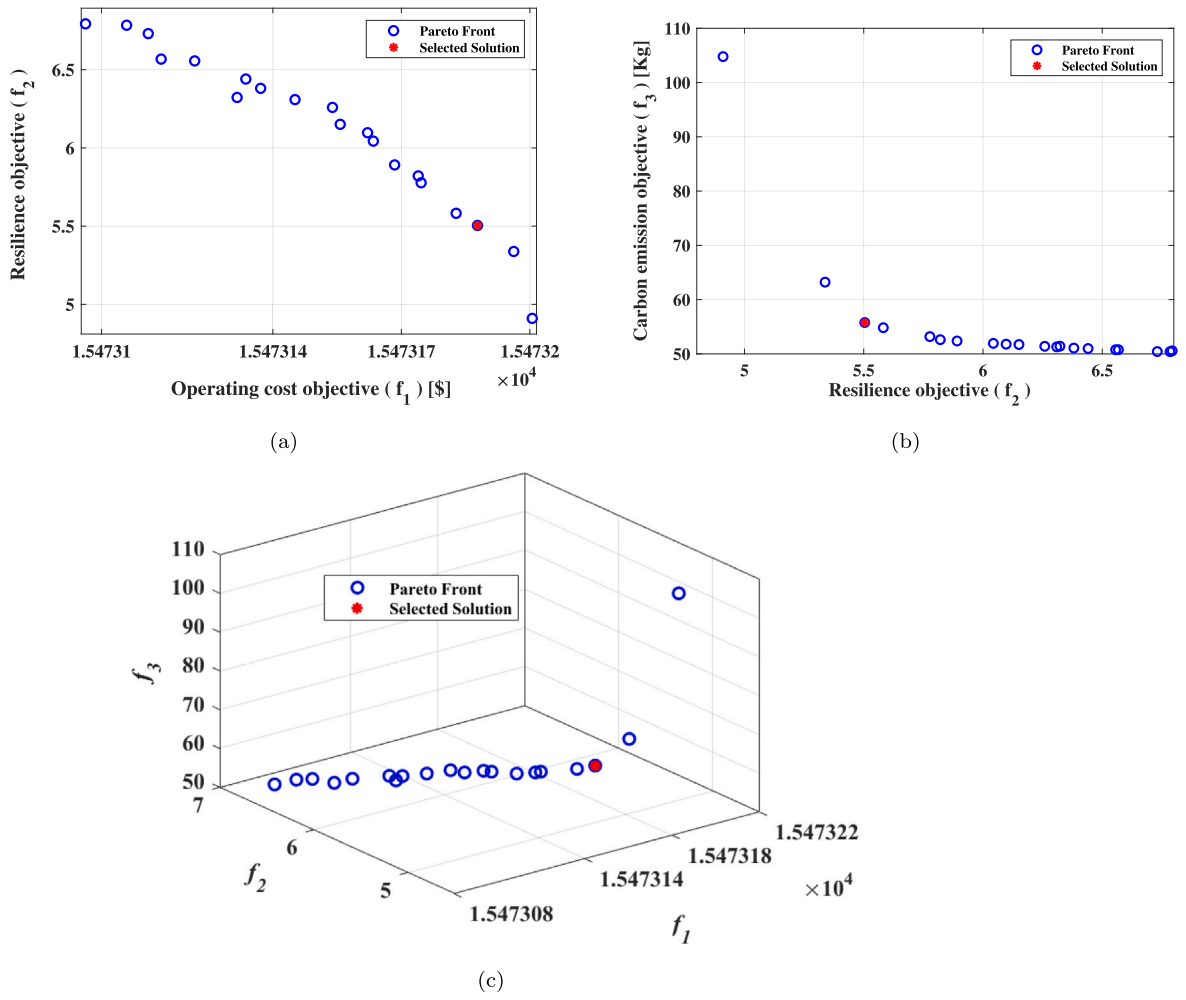

Fig. 11. The Pareto front of non-dominated solutions.

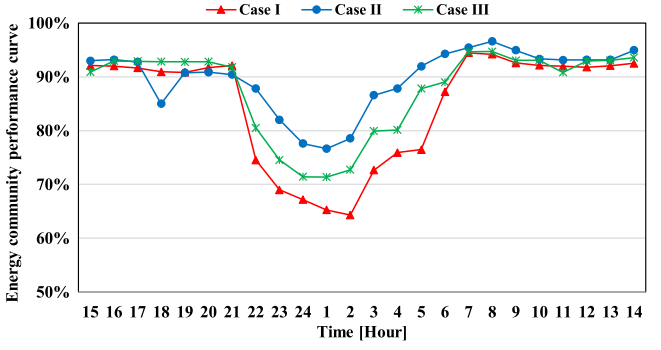

Fig. 12. The performance curve of the proposed energy community facing the extreme event in scenario 4.

the grid import and DG generation are minimized. This indicates a conscious effort to reduce carbon emissions while maintaining system functionality. On the other hand, in case II, both the DG generation and imported power are maximized. This is because the primary objective of the system is to enhance the resilience index. By maximizing both the DG generation and imported power, the system aims to ensure sufficient power supply and improve its ability to withstand and recover from disruptive events. As a result, Fig. 17 highlights the relationship between DG generation and imported power in scenario 4. During the event, the energy community operates independently, resulting in zero imported power. In case III, carbon emissions are minimized, leading to reduced grid import and DG generation. Conversely, in case II, both DG generation and imported power are maximized to enhance system resilience.

Fig. 18 represents the sum of the deviation in bus voltages, which serves as a technical metric. It is important to note that in all cases, the voltage buses are maintained within the range of 0.95 to 1.05 p.u. The figure illustrates the deviation of the bus voltages from the ideal value of 1 p.u.

Based on Fig. 18, it is evident that the voltage deviation remains low in cases II and III. This can be attributed to the fact that in these cases, the voltage deviation index (VDI) is considered a resilience metric and is integrated into the optimization objective function. As a result, the system is designed to prioritize voltage stability and minimize voltage deviations. In contrast, in case I, the voltage deviation notably increases during the event hours. This indicates that the system's resilience to voltage variations is compromised during this period, possibly due to limited contingency measures or suboptimal operation strategies. Furthermore, during normal operation hours, the VDI is higher in case III compared to cases I and II. This is primarily because case III takes into account carbon emissions and imposes limitations on both imported power and DG generation. Consequently, the system operates with reduced power resources, which can result in higher voltage deviations during normal operation hours. In summary, Fig. 18 reveals that cases II and III maintain low voltage deviations due to the inclusion of VDI as a resilience metric in the optimization objective. Conversely, case I experiences significant voltage deviations during the event hours.

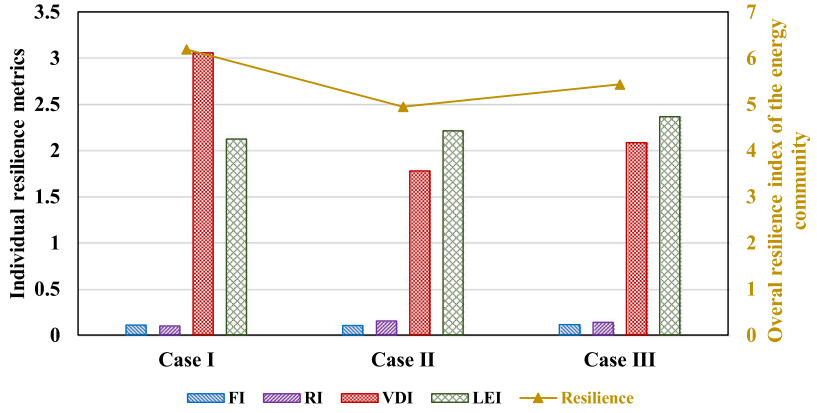

Fig. 13. The resilience metrics of the proposed energy community.

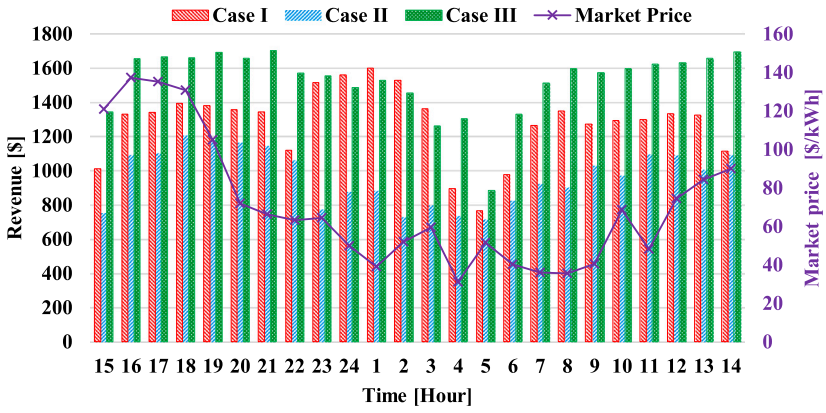

Fig. 14. The revenue chart of the proposed energy community in scenario 4.

Additionally, case III exhibits higher VDI during normal operation hours compared to cases I and II, as carbon emission constraints restrict imported power and DG generation.

4. Conclusions

This paper aims to develop a multi-objective economic-resilience-carbon emission stochastic scheduling mechanism for distributed energy resources (DERs) based energy communities (ECs), utilizing reconfiguration and effective load-carrying capability (ELCC) quantification. The key contribution of the proposed method lies in the integration of a mesh-view scheme, which captures the correlation between extreme event locations and energy community component locations within the mathematical formulations. By modeling the behavior of extreme events on the system and analyzing the correlation between event location and system components, the mesh-view approach enhances the understanding of extreme event impacts on ECs. To evaluate the proposed method, 5000 scenarios were initially generated, incorporating stochastic parameters such as event characteristics (i.e., location, severity level, and type), real-time market price, electric vehicle (EV) characteristics (i.e., arrival time, departure time, and arrival state of charge), and wind generation. To manage computational complexity, the number of scenarios was reduced to 10 using the k-means clustering method, implemented in MATLAB. Numerical simulation case studies have been demonstrated on the IEEE 33 bus test system, encompassing various DER units, including EVs, diesel generators, energy storage systems, and wind turbines. The simulation has been conducted and illustrated under three distinct cases, each based on different optimization objective functions and considering four different event types including storm, hurricane, earthquake, and ice freezing. The results highlighted the importance of an appropriate method for selecting the best solution for economic-resilience-carbon emission indices to achieve a balanced approach between resilience and economic metrics within low-carbon ECs. Specifically, energy storage and electric vehicle-to-grid (EVP) facilities demonstrated their significance in reducing operating costs through optimized charge/discharge behaviors during different market price hours and extreme events, consequently improving resilience. This trade-off between cost reduction and enhanced resilience presented a win-win situation for energy communities. Furthermore, the simulations showcased the substantial contribution of wind and distributed generation units in providing reliable power during emergencies following extreme events, further strengthening energy community resilience.

The findings of this study open up several potential avenues for future research in the field of resilient ECs. Further investigation can be conducted to incorporate advanced forecasting techniques and real-time data analysis for enhancing the accuracy of extreme event prediction and enabling more proactive decision-making in managing ECs during emergencies. The proposed framework can also consider multi-community interactions, enabling the analysis of resilience at a larger scale and facilitating coordination between neighboring communities. In addition, the economic and resilience metrics can be expanded to encompass social factors, enabling a more holistic evaluation of EC performance. These potential directions can contribute to the development of robust and adaptive ECs that effectively address the challenges posed by extreme weather events while promoting sustainability and resilience.

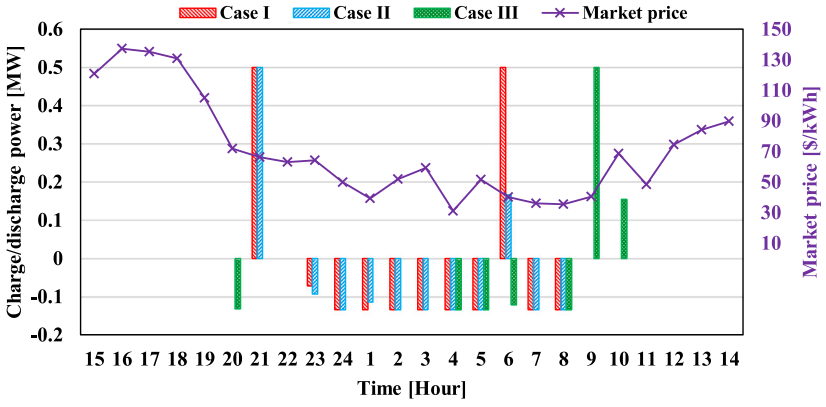

(a) EVP located at bus 33

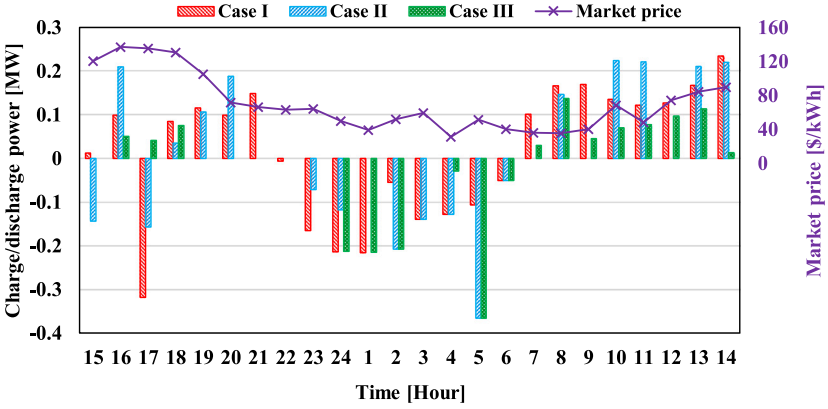

(b) ESS located at bus 26

Fig. 15. The charge/discharge behavior of EVP and ESS devices compared to real-time market price in scenario 4.

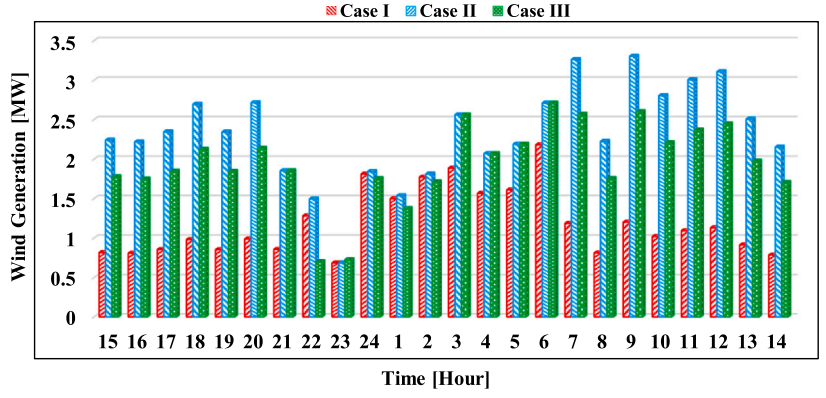

Fig. 16. The total wind generation in scenario 4.

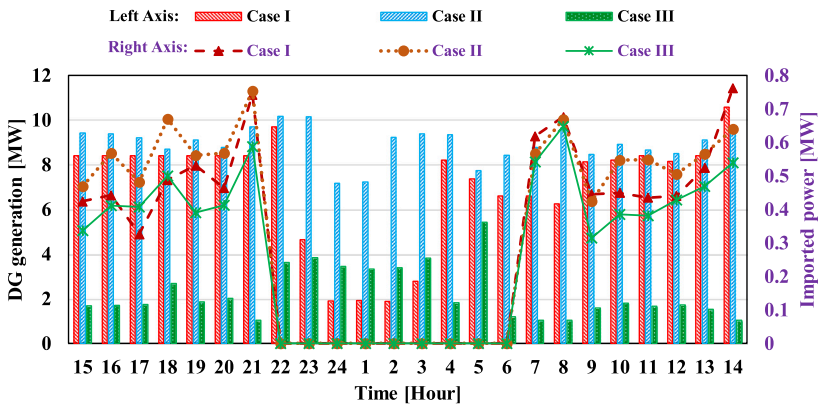

Fig. 17. The total DG generation vs. imported power in scenario 4.

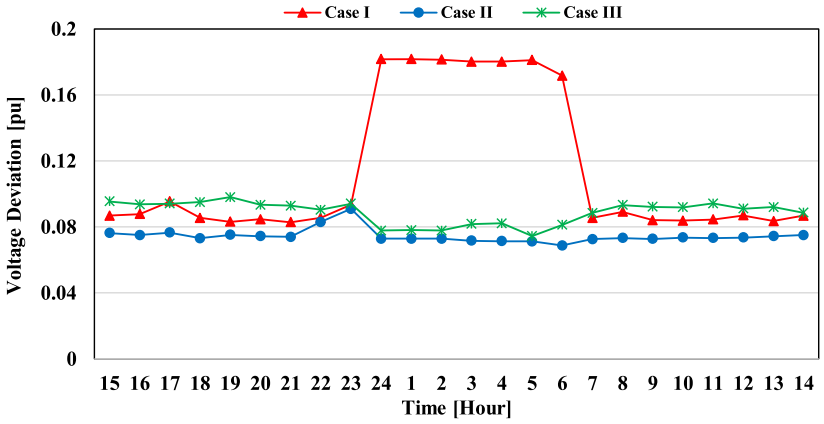

Fig. 18. The sum of deviation in the energy community bus voltages in scenario 4.

CRediT authorship contribution statement

Abdollah Younesi: Conceptualization, Methodology, Resources, Validation, Visualization, Writing – original draft. **Zongjie Wang:** Conceptualization, Funding acquisition, Methodology, Supervision, Validation, Visualization, Writing – original draft, Writing – review & editing. **Pierluigi Siano:** Validation, Visualization, Writing – review & editing.

Declaration of competing interest

The authors declare that they have no known competing financial interests or personal relationships that could have appeared to influence the work reported in this paper.

Data availability

The data that has been used is confidential.

Acknowledgment

This work was funded in part by the Eversource project entitled "A Pathway to Enhance Grid Resilience: Zero-Carbon Energy Communities with DER-based ELCC Quantification" (PI: Wang). This work was also funded in part by the BNL project entitled "Solar PLUS: Solar Integration through Physics-Aware Learning Based Ultra-Scalable Modeling and Analytics" (Project No. : 431421, PI: Wang). Pierluigi Siano was supported by a grant from the Ministry of Research, Innovation, and Digitalization, project number PNRR-C9-I8-760090/23.05.2023, code CF 30/14.11/2022.

All authors approved the version of the manuscript to be published.

References

Cagnano, A., De Tuglie, E., Mancarella, P., 2020. Microgrids: Overview and guidelines for practical implementations and operation. Appl. Energy 258, 114039.

Chamana, M., Schmitt, K.E.K., Bhatta, R., Liyanage, S., Osman, I., Murshed, M., Bayne, S., MacFie, J., 2022. Buildings participation in resilience enhancement of community microgrids: Synergy between microgrid and building management systems. IEEE Access 10, 100922–100938.

Chen, Z., Wu, L., Shahidehpour, M., 2014. Effective load carrying capability evaluation of renewable energy via stochastic long-term hourly based SCUC. IEEE Trans. Sustain. Energy 6 (1), 188–197.

Coffrin, C., Van Hentenryck, P., 2014. A linear-programming approximation of AC power flows. INFORMS J. Comput. 26 (4), 718–734.

Dent, C.J., Hernandez-Ortiz, A., Blake, S.R., Miller, D., Roberts, D., 2014. Defining and evaluating the capacity value of distributed generation. IEEE Trans. Power Syst. 30 (5), 2329–2337.

Garver, L.L., 1966. Effective load carrying capability of generating units. IEEE Trans. Power Apparatus and Syst. (8), 910–919.

Gholami, A., Aminifar, F., 2015. A hierarchical response-based approach to the load restoration problem. IEEE Trans. Smart Grid 8 (4), 1700–1709.

Guo, Z., Li, G., Zhou, M., Feng, W., 2019. Resilient configuration approach of integrated community energy system considering integrated demand response under uncertainty. Ieee Access 7, 87513–87533.

Hajagos, L.M., Danai, B., 1998. Laboratory measurements and models of modern loads and their effect on voltage stability studies. IEEE Trans. Power Syst. 13 (2), 584–592.

Harrison, G.P., Piccolo, A., Siano, P., Wallace, A.R., 2007. Exploring the tradeoffs between incentives for distributed generation developers and DNOs. IEEE Trans. Power Syst. 22 (2), 821–828.

Heath, B., Figueroa-Acevedo, A.L., 2018. Potential capacity contribution of renewables at higher penetration levels on MISO system. In: 2018 IEEE International Conference on Probabilistic Methods Applied to Power Systems. PMAPS, IEEE, pp. 1–6.

Lazaroiu, G.C., Putrus, G., 2023. Renewable energy generation driving positive energy communities. Renew. Energy.

Mahzarnia, M., Moghaddam, M.P., Baboli, P.T., Siano, P., 2020. A review of the measures to enhance power systems resilience. IEEE Syst. J. 14 (3), 4059–4070.

Midcontinent-ISO, 2015. MISO Tariff, Module E-1 – Resource Adequacy. Midcontinent ISO.

Nagpal, H., Avramidis, I.-I., Capitanescu, F., Madureira, A.G., 2022. Local energy communities in service of sustainability and grid flexibility provision: Hierarchical management of shared energy storage. IEEE Trans. Sustain. Energy 13 (3), 1523–1535.

Osman, A.I., Chen, L., Yang, M., Msigwa, G., Farghali, M., Fawzy, S., Rooney, D.W., Yap, P.-S., 2023. Cost, environmental impact, and resilience of renewable energy under a changing climate: A review. Environ. Chem. Lett. 21 (2), 741–764.

Papari, B., Edrington, C.S., Ghadamyari, M., Ansari, M., Ozkan, G., Chowdhury, B., 2021. Metrics analysis framework of control and management system for resilient connected community microgrids. IEEE Trans. Sustain. Energy 13 (2), 704–714.

Poudyal, A., Poudel, S., Dubey, A., 2022. Risk-based active distribution system planning for resilience against extreme weather events. IEEE Trans. Sustain. Energy.

Putratama, M.A., Rigo-Mariani, R., Mustika, A.D., Debusschere, V., Pachurka, A., Besanger, Y., 2022. A three-stage strategy with settlement for an energy community management under grid constraints. IEEE Trans. Smart Grid.

Quijano, D.A., Padilha-Feltrin, A., 2019. Optimal integration of distributed generation and conservation voltage reduction in active distribution networks. Int. J. Electr. Power Energy Syst. 113, 197–207.

Rahiminejad, A., Ghafouri, M., Atallah, R., Lucia, W., Debbabi, M., Mohammadi, A., 2023. Resilience enhancement of islanded microgrid by diversification, reconfiguration, and DER placement/sizing. Int. J. Electr. Power Energy Syst. 147, 108817.

Tomin, N., Shakirov, V., Kozlov, A., Sidorov, D., Kurbatsky, V., Rehtanz, C., Lora, E.E., 2022. Design and optimal energy management of community microgrids with flexible renewable energy sources. Renew. Energy 183, 903–921.

Trodden, P.A., Bukhsh, W.A., Grothey, A., McKinnon, K.I., 2013. Optimization-based islanding of power networks using piecewise linear AC power flow. IEEE Trans. Power Syst. 29 (3), 1212–1220.

Utkarsh, K., Ding, F., Jin, X., Blonsky, M., Padullaparti, H., Balamurugan, S.P., 2021. A network-aware distributed energy resource aggregation framework for flexible, cost-optimal, and resilient operation. IEEE Trans. Smart Grid 13 (2), 1213–1224.

Vagropoulos, S.I., Bakirtzis, A.G., 2013. Optimal bidding strategy for electric vehicle aggregators in electricity markets. IEEE Trans. Power Syst. 28 (4), 4031–4041.

Vespermann, N., Hamacher, T., Kazempour, J., 2020. Access economy for storage in energy communities. IEEE Trans. Power Syst. 36 (3), 2234–2250.

Wang, Y., Chen, C., Wang, J., Baldick, R., 2015. Research on resilience of power systems under natural disasters—A review. IEEE Trans. Power Syst. 31 (2), 1604–1613.

Younesi, A., Shayeghi, H., Safari, A., Siano, P., 2020. Assessing the resilience of multi microgrid based widespread power systems against natural disasters using Monte Carlo simulation. Energy 207, 118220.

Younesi, A., Shayeghi, H., Siano, P., Safari, A., 2021a. A multi-objective resilience-economic stochastic scheduling method for microgrid. Int. J. Electr. Power Energy Syst. 131, 106974.

Younesi, A., Shayeghi, H., Siano, P., Safari, A., Alhelou, H.H., 2021b. Enhancing the resilience of operational microgrids through a two-stage scheduling strategy considering the impact of uncertainties. IEEE Access 9, 18454–18464.

Younesi, A., Shayeghi, H., Wang, Z., Siano, P., Mehrizi-Sani, A., Safari, A., 2022a. Trends in modern power systems resilience: State-of-the-art review. Renew. Sustain. Energy Rev. 162, 112397.

Younesi, A., Wang, Z., Nguyen, H.T., Mandal, P., 2022b. A pathway to enhance the modern distribution systems resilience: Flexible behavior investigations on electric vehicles. In: 2022 IEEE Power & Energy Society General Meeting. PESGM, IEEE, pp. 01–05.

Younesi, A., Wang, Z., Siano, P., Wang, F., 2023. A pathway to mitigate climate change impacts on energy communities: Decarbonization-based cost-effective grid resilience enhancement. In: 2023 IEEE Power & Energy Society General Meeting. PESGM, IEEE, pp. 1–5.

Younesi, A., Wang, Z., Wang, L., 2022c. Investigating the impacts of climate change and natural disasters on the feasibility of power system resilience. In: 2022 IEEE Power & Energy Society General Meeting. PESGM, IEEE, pp. 1–5.

Zakariazadeh, A., Jadid, S., Siano, P., 2014. Stochastic multi-objective operational planning of smart distribution systems considering demand response programs. Electr. Power Syst. Res. 111, 156–168.